The Cryosphere

EGU Open Access

Five decades of Abramov glacier dynamics reconstructed with multi-sensor optical remote sensing

Enrico Mattea[1], Etienne Berthier[2], Amaury Dehecq[3], Tobias Bolch[4,8], Atanu Bhattacharya[5,6], Sajid Ghuffar[7], Martina Barandun[1], and Martin Hoelzle[1]

[1]Department of Geosciences, University of Fribourg, Fribourg, Switzerland
[2]LEGOS, Université de Toulouse, CNES, CNRS, IRD, UT3, Toulouse, France
[3]Univ. Grenoble Alpes, IRD, CNRS, INRAE, Grenoble INP, IGE, 38000 Grenoble, France
[4]Institute of Geodesy, Graz University of Technology, Graz, Austria
[5]Department of Earth Sciences and Remote Sensing, JIS University, Kolkata, India
[6]Centre for Data Science, JIS Institute of Advanced Studies and Research, Kolkata, India
[7]Department of Space Science, Institute of Space Technology, Islamabad, Pakistan
[8]Central Asian Regional Glaciological Centre, Category 2 centre under the auspices of UNESCO, Almaty, Kazakhstan

Correspondence: Enrico Mattea (enrico.mattea@unifr.ch)

Abstract. Reference glacier sites with systematic in situ monitoring provide crucial information to understand trends in regional change. Throughout Central Asia, several sites have been established over the past 15 years, often restarting long-term time series interrupted after the Soviet Union's collapse. The region also features widespread ice flow instabilities, including surge-type glaciers. Unstable ice dynamics have been usually observed within large-scale remote sensing studies, with limited ground validation or historical observations. This hampers interpretation of the driving factors of glacier change, their interaction with mass balance, and regional representativity of single glaciers. Here, we reconstruct ice dynamics at the reference Abramov glacier using satellite-based optical remote sensing. The glacier, monitored in situ over 1967–1999 and again since 2011, experienced a well-documented episode of fast flow in 1972–1973. We compile a 55-year dataset of digital elevation models (DEMs) and orthoimages by processing raw and analysis-ready imagery from multiple archives, including declassified reconnaissance satellites, the Satellite Pour l'Observation de la Terre (SPOT), and RapidEye. Our estimates for glacier length and volume changes agree well with previous observational, remote sensing, and model studies. We describe at subseasonal scale a second pulsation over 2000–2005 – not observed in situ and poorly resolved by Landsat and ASTER products. We also measure the buildup to a third velocity pulsation, with doubling of mean annual velocity since 2011 despite a continued mass loss of -0.55 ± 0.06 m w.e. yr^{-1}. The collected evidence indicates that Abramov is a surge-type glacier with a recurrence time of 20–30 years, challenging its representativity for regional mass balance. However, we also find a decreasing magnitude and increasing duration of the pulsations, suggestive of a potential ongoing transition towards more stable dynamics.

1 Introduction

Glaciers are an essential component of the hydrological cycle in Central Asia, providing a large fraction of the runoff during the dry summer months – a critical contribution for diverse sectors such as agriculture or hydropower production (Huss and Hock, 2018; Hoelzle et al., 2019). At the same time, the vast glacierization across Tien Shan and Pamir, in High Mountain Asia, presents a multitude of glacier-related hazards such as collapses and glacial lake outburst floods (GLOFs), which can significantly damage settlements and livelihoods (Komatsu and Watanabe, 2014; Muccione and Fiddes, 2019). Accelerated climate change is impacting glaciers in Central Asia, leading to significant changes

in runoff patterns and hazard potential, with consequences still largely uncertain (Unger-Shayesteh et al., 2013; Xenarios et al., 2019; Barandun et al., 2020). Therefore, both long-term monitoring and improved process understanding are crucial to reduce the current uncertainties (Barandun et al., 2020).

The Soviet Union maintained an extensive monitoring program on reference glacier sites in Central Asia, resulting in a comprehensive observational dataset on mass balance, meteorology, hydrology, and ice dynamics. Following the fall of the Soviet Union, this monitoring was mostly discontinued during the 1990s (Unger-Shayesteh et al., 2013); however, annual monitoring has been progressively reestablished since 2010 at several sites, providing valuable continuation to long-term measured time series, especially of meteorological variables and glacier mass balance (Schöne et al., 2013; Hoelzle et al., 2017; Barandun et al., 2018). The observational gap in the mass balance records for individual reference glaciers has been addressed with multiple methods, including geodetic estimation (Denzinger et al., 2021), parameterized approaches such as temperature-index models (Barandun et al., 2015; Kronenberg et al., 2016; Kenzhebaev et al., 2017; Barandun et al., 2018; Popovnin et al., 2021; Van Tricht et al., 2021; Azisov et al., 2022), and full energy-balance simulations (Kronenberg et al., 2022). Moreover, several regional- and global-scale studies have also estimated mass balance for most or all glaciers in Central Asia, using satellite-based remote sensing to derive surface elevation changes and/or constrain large-scale modeling (Gardner et al., 2013; Gardelle et al., 2013; Farinotti et al., 2015; Kääb et al., 2015; Brun et al., 2017; Zemp et al., 2019; Shean et al., 2020; Hugonnet et al., 2021; Barandun et al., 2021; Fan et al., 2023). Yet, Barandun and Pohl (2023) found data inconsistencies and regional simplifications that hinder interpretation and attribution of the trends shown in such large-scale datasets, and the time series from reference sites remain crucial for a better understanding of the changing Central Asia cryosphere.

Mass balance representativity of reference glaciers can be affected by their ice dynamics (Oerlemans and Van Pelt, 2015; Lv et al., 2020b). The mountains of Central Asia present a high prevalence of glaciers with unstable ice flow (Sevestre and Benn, 2015; Mukherjee et al., 2017; Goerlich et al., 2020; Guillet et al., 2022), known as pulsating glaciers in Soviet literature and as surge-type glaciers in Western terminology (Jiskoot, 2011). Such glaciers periodically alternate between active phases of accelerated flow, with downstream mass redistribution from a reservoir area, and longer stretches of quiescent recovery, marked by lower ice velocities. The cycle is driven by an intrinsic dynamic instability (Meier and Post, 1969; Sevestre and Benn, 2015), although climatic forcing and mass balance can partly shape the characteristics and duration of the active phase (Emelyanov et al., 1974; Eisen et al., 2001; Hewitt, 2007; Flowers et al., 2011; Pitte et al., 2016). The inventory of surge-type glaciers in High Mountain Asia compiled by Guillet et al. (2022) reports active phases lasting 1 to 18 years (median = 2 years, $N = 30$) in Tien Shan and 1 to 19 years (median = 3 years, $N = 73$) in the Pamirs. Information on recurrence intervals of surging activity is scarce in that inventory and other inventories, because usually a single surge cycle takes place during the considered time interval. Reported values range from 1 to 5 decades (Murodov et al., 2024; Mukherjee et al., 2017).

Several mechanisms have been proposed to explain the occurrence of glacier surges (Kamb, 1987; Fowler et al., 2001; Harrison and Post, 2003; Benn et al., 2019; Thøgersen et al., 2019; Terleth et al., 2021); yet, unstable ice dynamics in Central Asia appear to elude classification according to the classical models (Quincey et al., 2015; Chudley and Willis, 2019; Lv et al., 2020a). Moreover, differentiation between a surge and an advance is not always straightforward (Paul, 2015; Lv et al., 2020a), as a continuous spectrum of flow instabilities is assumed to exist between the stable and surge-type end-members (Mayo, 1978; Jiskoot, 2011; Herreid and Truffer, 2016). Unstable glaciers present challenges for the monitoring and interpretation of mass balance trends (Bhambri et al., 2017). Glacier-wide mass balance can fluctuate from a positive anomaly before the active phase to a negative one immediately after, as the glacier abruptly advances to lower and warmer locations (Lv et al., 2020b; King et al., 2023). The altitudinal mass balance gradient tends to be too steep during quiescence, compensated for by downward mass redistribution during the active phase (Dolgoushin and Osipova, 1975; Raymond, 1987; Lv et al., 2020b). Increased water storage within and beneath the glacier can significantly affect geodetic mass balance estimations (Raymond, 1987; Humphrey and Raymond, 1994). Rapid evolution of the surface – for example, area, slope, and albedo affecting the energy balance – is not easily accounted for within model studies (Emelyianov et al., 1974; Kronenberg et al., 2022). Finally, the monitoring network can be damaged or become inaccessible during the active phase, which can be especially problematic for sites with complex logistics or infrequent revisits (Emelyianov et al., 1974). Therefore, mass balance trends of surge-type glaciers are generally recognized as representative only over a timescale longer than one surge cycle, and these glaciers are usually excluded from (or treated separately within) geodetic estimates of regional mass balance (Gardelle et al., 2013; Zhou et al., 2019; Lv et al., 2020b).

A key reference site in Central Asia potentially affected by unstable ice dynamics is Abramov (39°37′ N, 71°33′ E; Fig. 1), a valley glacier in the Pamir-Alay mountains of Kyrgyzstan covering 21 km^2 as of 2024. Between 1967 and 1999, the Abramov glacier was monitored year-round at a dense network of point measurements, resulting in a detailed dataset of meteorological, glaciological, and hydrological observations (Suslov et al., 1980; Glazirin' et al., 1993; Pertziger, 1996). Glacier-wide calculations by various authors have indicated a mean mass loss of 0.4 to

$0.7\,\mathrm{m\,w.e.\,yr^{-1}}$ over the monitored period, with almost no year of mass gain (Barandun et al., 2015). Between 1972 and 1973, after several years of acceleration, the glacier experienced a pulsation: surface velocity increased up to 5-fold and the terminus advanced more than 400 m, with a maximum velocity of $2\,\mathrm{m\,d^{-1}}$ (Emelyianov et al., 1974; Kotlyakov et al., 2017). Flow velocity on the glacier tongue peaked in June 1973, before entering a rapid decline down to a minimum reached in early 1974 (Abulkhasanova et al., 1979; Suslov et al., 1980). This low-intensity event was characterized as a quiet pulsation, with relatively minor mass redistribution along the glacier, as opposed to stronger traditional surges (Glazirin', 1978; Mayo, 1978; Glazirin' and Shchetinnikov, 1980; Van Wychen et al., 2016). Soviet and Russian publications have reported somewhat contrasting measurements for this event, including terminus retreat in the preceding years, total advance during the active phase, ice volume transferred to the tongue, and estimated recurrence time (Emelyianov et al., 1974; Suslov et al., 1980; Dolgoushin and Osipova, 1982; Glazirin' et al., 1993; Kotlyakov et al., 2017); still, all agree on the general characteristics. Using a minimal flow-line model, Glazirin' et al. (1987) investigated the pulsation with various formulations of the basal sliding law. The best agreement with observed ice velocities was found by introducing a switch in the friction coefficient between two different values, as controlled by a threshold of basal shear stress: as such, the authors attributed the pulsation to a sudden shift in basal conditions, but the mechanism of such a shift was not examined. The subsequent recovery period lasted into the 1990s, with slow and regular ice flow and widespread thickness loss over the glacier tongue (Abulkhasanova et al., 1979; Suslov et al., 1980; Grishin and Abulkhasanova, 1986; Glazirin' et al., 1993). The Abramov research station was abandoned in 1999 (Savoskul, 2000), and the glacier went unobserved until 2011, when annual mass balance monitoring was resumed and an automatic weather station (AWS) was installed (Schöne et al., 2013; Hoelzle et al., 2017). Unlike for mass balance, the gap in ice dynamics measurements has not been addressed so far, and systematic monitoring has not been reestablished.

Here we reconstruct 55 years of unstable ice flow at Abramov with satellite-based optical remote sensing. We find that existing satellite-based datasets such as Landsat and ASTER fail for the most part to resolve ice dynamics at Abramov, and thus we process several scenes from multiple higher-resolution sensors, such as the Indian Remote Sensing (IRS-1C/D) program (Kasturirangan et al., 1996), the Satellite Pour l'Observation de la Terre (SPOT; Riazanoff, 2002), and the RapidEye constellation (Tyc et al., 2005). We measure changes in glacier thickness, velocity, and terminus position, describing a second unobserved pulsation in the early 2000s and the buildup to a third one during the 2010s and early 2020s.

2 Materials and methods

2.1 Analysis-ready data

Several orthoimages and topographic datasets are available for Abramov glacier from public archives and previous studies (Table 1). We downloaded all Level-1C orthoimages available from the Sentinel-2 repository (Drusch et al., 2012) between 2015 and 2023, specifically bands 2, 3, 4, and 8 at 10 m resolution. The entire glacier surface is covered by two relative orbits (91 and 134), providing four revisits every 10 d since 2017. We used these scenes to derive ice surface velocities at annual intervals (Sect. 2.3.2) using frequency-domain correlation (Leprince et al., 2007). We also collected the data from Denzinger et al. (2021) – orthoimages and DEMs of the glacier obtained from scanned aerial frames from 1975 – and a submeter stereo pair captured by Pléiades in 2015 (Berthier et al., 2024). From Hugonnet et al. (2021), we obtained a set of 11 DEMs generated at 30 m resolution out of all ASTER stereo pairs (NASA/METI/AIST/Japan Spacesystems and U.S./Japan ASTER Science Team, 2001); four such DEMs are cloud- and snow-free at Abramov and cover the early 2000s. In addition, we retrieved elevation grids from two radar-derived global DEMs: Copernicus (European Space Agency and Airbus, 2022) and NASADEM (NASA JPL, 2020). The Copernicus DEM is downsampled from higher-resolution data and shows better detail and lower error metrics than those from NASADEM when compared with reference measurements (Fahrland, 2022; Li et al., 2022; Okolie et al., 2024). However, a large-scale elevation artifact in the vicinity of Abramov glacier prevents direct use of this DEM within comparisons of surface change, and thus we chose to use it only (in the GLO-30 and GLO-90 versions) as initial seed for stereo DEM generation. Conversely, NASADEM provides surface elevation data from February 2000 with somewhat higher noise but no apparent artifacts, and thus we chose to use it (1) to compute local changes in ice thickness, (2) as coregistration reference for all DEMs, and (3) to provide the topography for orthorectification of monoscopic scenes.

In addition to surface DEMs, bed elevation for the Abramov glacier is also known: Kuz'michenok et al. (1992) compiled a topographic map at a scale of 1 : 25 000, depicting the bed with contour lines at 10 m intervals. The original data were computed by combining the surface topography (measured by aerial survey) with a dense array of ice thickness measurements collected by radio-echo sounding in 1986. We georeferenced this map using 20 ground control points (GCPs) manually extracted from the 2015 Pléiades DEM, and we then digitized all contour lines and interpolated them into a bed DEM at 30 m resolution, using regularized spline with tension (Mitášová and Hofierka, 1993).
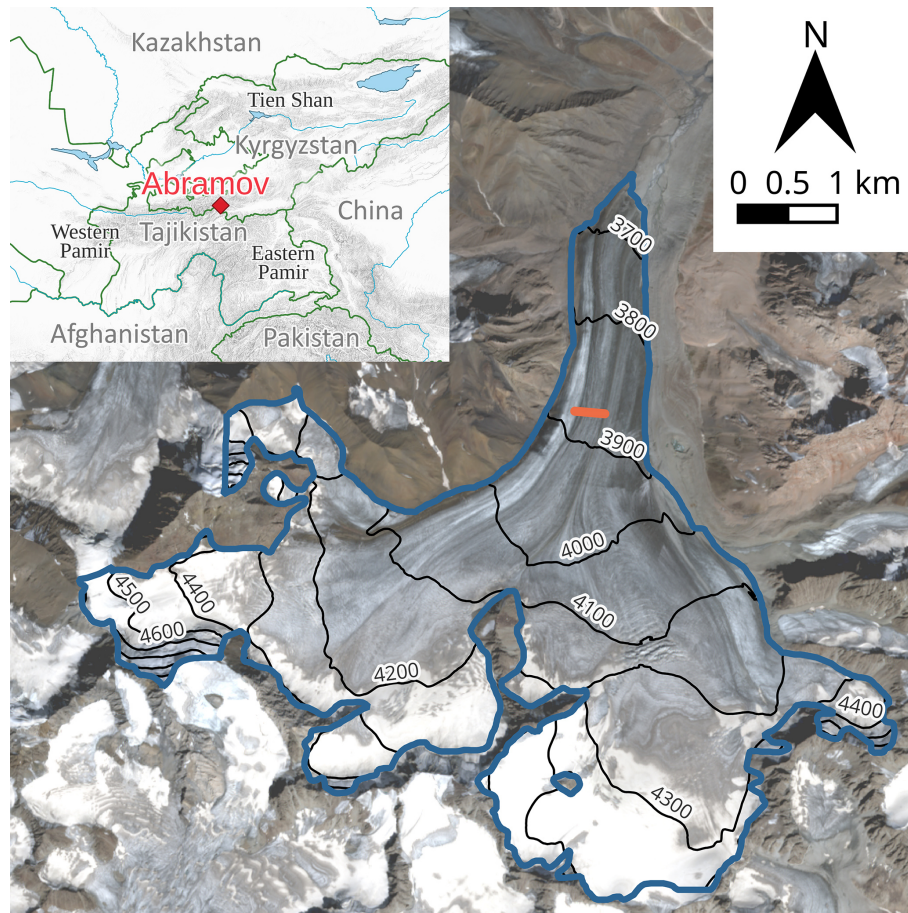
Figure 1. Location and detail maps of Abramov glacier. Background: Sentinel-2 multispectral instrument (MSI) natural color acquired on 5 September 2022. Elevation contours: Pléiades digital elevation model (DEM) from 5 September 2022. Glacier outline: manually digitized from Pléiades orthoimage of 5 September 2022. The orange line indicates transverse profile 4 of the historical monitoring network.

2.2　Newly produced datasets

We found that existing datasets do not provide an adequate level of detail to accurately reconstruct the dynamics of a relatively small and slow-moving glacier such as Abramov, especially for the period of interrupted monitoring (Appendix E). Therefore, we processed additional archived satellite scenes from multiple sensors to improve the spatiotemporal coverage of both orthoimages and DEMs.

We collected 35 monoscopic scenes from SPOT satellites 1 through 5, acquired between 1986 and 2013 and openly distributed since 2020 within the SPOT World Heritage (SWH) program (Nosavan et al., 2020). The scenes have a radiometric resolution of 8 bit and a nominal spatial resolution at nadir of 20 m (SPOT 1–4 in multispectral mode), 10 m (SPOT 1–4 in panchromatic mode; SPOT 5 multispectral), and 5 m (SPOT 5 panchromatic). We obtained 14 panchromatic scenes by IRS-1C/D through the Antrix Corporation Limited (Antrix Corporation Limited, 2019) recorded at 5.7 m pixel size and 6 bit depth between 1997 and 2006. Finally, we obtained 11 raw multispectral scenes from the

RapidEye constellation (Tyc et al., 2005) through the Education and Research Program of Planet Labs (Planet Labs, 2024). The scenes feature 6.5 m resolution at 12 bit and cover the period 2010–2019. Processing of all monoscopic scenes is described in Sect. 2.2.1.

For DEM generation (Sect. 2.2.2), we processed 18 stereo pairs from the SPOT 5 high-resolution stereoscopic (HRS) instrument, also distributed through the SWH program, covering the period from 2003 to 2006. These images feature rectangular pixels with a nominal ground sampling distance of 5 by 10 m. For the period of the 1970s pulsation, we produced DEMs and orthoimages from five stereo and two tristereo KH-4B and KH-9 panoramic camera (PC) and mapping camera (MC) scenes, acquired between 1968 and 1980 within the US spy satellite programs Corona and Hexagon (Table A2). The declassified film scans are available from the US Geological Survey (Earth Resources Observation And Science (EROS) Center, 2017a, b, c). Finally, we processed four additional Pléiades stereo pairs at 50 cm resolution ac-

quired between 2020 and 2023. All newly processed datasets are presented in Table 2.

2.2.1 Orthorectification of monoscopic scenes

We produced orthoimages from SPOT, IRS, and RapidEye with different tools, depending on the supporting metadata available within each dataset. We used the 50 cm Pléiades scene from September 2020 as reference for horizontal alignment, owing to its minimal cloud and snow cover. This scene extends over the region of Abramov glacier with a footprint of approximately 18 by 20 km.

The monoscopic SPOT scenes were orthorectified over the NASADEM terrain using the SPOT-specific rigorous sensor model (RSM) of Aati et al. (2022), as implemented in the open-source geoCosiCorr3D package. This method involves refinement of image geometry using GCPs to correct errors associated with the satellite viewing parameters reported in the scene metadata (Leprince et al., 2007; Aati et al., 2022). Technical details on SPOT orthorectification, including our adaptations of the pipeline of Aati et al. (2022), are described in Appendix B.

We received scenes from IRS-1C/D in raw format, with basic geometric corrections but no metadata or information on satellite viewing parameters. We orthorectified them using the sensor model of Toutin (2004), as implemented in Catalyst Professional Orthoengine (PCI Geomatics Enterprises, 2024). After providing a coarse geolocation from five manual GCPs, we used a 2006 SPOT 5 HRG orthoimage as reference for automatic GCP generation. We applied the Smallest Univalue Segment Assimilating Nucleus (SUSAN) algorithm (Smith and Brady, 1997) for feature point detection and then fast Fourier transform phase matching (Kuglin and Hines, 1975) for tie point calculation. Subsequent orthorectification is basically independent of the manual choice of initial GCPs. We produced final orthoimages at 5 m resolution.

Finally, RapidEye scenes were orthorectified by means of the mapproject tool from the NASA Ames Stereo Pipeline (ASP; Beyer et al., 2018), based on the rational polynomial coefficient (RPC) information provided within each product. We used the image_align tool from the same software package to apply fine registration of each orthoimage to the SPOT 5 HRG reference, with a rigid transform estimated from interest point matching with singular value decomposition.

2.2.2 Stereo processing

We processed stereo scenes into DEMs and orthoimages, in most cases, using the open-source tools from ASP, with specific processing steps and parameters adapted to the characteristics of each stereo dataset. The only exceptions were the three scenes acquired by panoramic cameras aboard the KH-4B and KH-9 satellites (Table 2). Due to the complex acquisition geometry, we processed the KH-4B data with the Re-

mote Sensing Software Package Graz (RSG) using the methods in Bhattacharya et al. (2021) and the KH-9 PC scenes according to Ghuffar et al. (2022, 2023). Spatial resolution of the original images is 1.8 and 0.6 m for KH-4B and KH-9, respectively. We also processed imagery from the mapping camera aboard KH-9, with the automated method in Dehecq et al. (2020), again based on NASA ASP. KH-9 PC and MC acquisition dates do not match (Table 2) because the two systems were not usually operated at the same time.

We produced 15 DEMs from the SPOT 5 HRS stereo pairs at 30 m resolution. We ran stereo correlation with the more global matching (MGM) algorithm (Facciolo et al., 2015) as implemented in NASA ASP and the processing parameters of Shugar et al. (2021) and Bhushan and Shean (2021). In four scenes the glacier is split over two pairs, which we mosaicked into single DEMs. Our dataset also includes four instances of repeat HRS acquisitions at an interval of just 5 d. The corresponding DEM pairs were used to verify the stability of our results on glacier terrain by measuring the mean change in surface height over the outlines of the Randolph Glacier Inventory (RGI) version 7 (RGI 7.0 Consortium, 2023). Further methodological details on SPOT DEM generation are described in Appendix C.

Finally, we generated Pléiades DEMs at 4 m resolution for September 2020, 2022, and 2023. We used the semi-global matching (SGM) algorithm with parameters from Deschamps-Berger et al. (2020) both for consistency with the 2015 Pléiades DEMs of Barandun et al. (2018) and for a lower computational cost compared to that of MGM (each scene includes more than 10^9 pixels). We then orthorectified the raw panchromatic images over their respective DEM surfaces using the provided RPC metadata to a final pixel size of 0.5 m. The 2022 dataset consists of two half pairs split longitudinally, which we mosaicked with the same methods as for HRS (Appendix C).

2.3 Derivation of glaciological parameters

2.3.1 Glacier terminus mapping

We manually digitized the terminus of Abramov glacier on all cloud-free orthoimages in our dataset; availability of a single band (in most cases) prevented the application of automated ice mapping methods, which would require, in any case, manual corrections to obtain the highest accuracy (Racoviteanu et al., 2009; Paul et al., 2015). We used the digitized outlines as regions of interest to compute changes in ice volume and applied the rectilinear box method to compute evolution of the width-averaged glacier length (Moon and Joughin, 2008; Lea et al., 2014). To quantify length uncertainty from residual misregistration and distortions, the method was repeated on two ostensibly stable features: a rock ridge and an unpaved road (Fig. 2b). The two features have similar length to the width of the glacier terminus; are located within 1 km of it; and, being almost perpendicular,

Table 1. Analysis-ready data from previous studies and public archives. HiRI: high-resolution imager. MSI: multispectral instrument. PAN: single-band panchromatic. Global DEMs (NASADEM and Copernicus) are provided in equirectangular projection, defined in arc-second units: in the mid-latitudes their resolutions of $1''$ and $3''$ are often assumed to correspond to 30 and 90 m, respectively.

Data type	Platform and sensor	Resolution	Time coverage	Notes	References
Orthoimage	Aerial, AFA-TES camera	2 m	12 July 1975		Denzinger et al. (2021)
	Pléiades HiRI PAN	0.5 m	1 September 2015		Barandun et al. (2018)
	Sentinel-2 MSI	10 m	2015–2023	Bands 2/3/4/8	Drusch et al. (2012)
DEM	Aerial, AFA-TES camera	4 m	12 July 1975		Denzinger et al. (2021)
	Terra ASTER	30 m	2001–2006		Hugonnet et al. (2021)
	Space Shuttle, radar (C-band)	$1''$	February 2000	NASADEM	NASA JPL (2020)
	Pléiades HiRI	4 m	1 September 2015		Barandun et al. (2018)
	TanDEM-X, radar (X-band)	$1''$, $3''$	2011–2015	Copernicus GLO-30 and GLO-90	European Space Agency and Airbus (2022)

Table 2. Newly processed satellite datasets. GSD: best-case ground sampling distance of raw scenes. PC: panoramic camera. MC: mapping camera (tristereo). HRS: high-resolution stereoscopic. HRV: high-resolution visible. HRVIR: high-resolution visible and infrared. HRG: high-resolution geometric. REIS: RapidEye Earth-imaging System. PAN: single-band panchromatic. MS: multispectral.

Data type	Platform	Sensor	GSD [m]	Time coverage	Count
Stereo pairs	Corona	KH-4 PC	1.8	18 August 1968	1
	Hexagon	KH-9 MC	6	1973–1980	3
	Hexagon	KH-9 PC	0.6	1972–1980	3
	SPOT 5	HRS	5×10	2003–2011	18
	Pléiades	HiRI PAN	0.5	2020–2023	4
Mono scenes	SPOT 1	HRV MS	20	1986	1
	SPOT 3	HRV PAN	10	1996	1
	SPOT 4	HRVIR PAN and MS	10 and 20	1999–2003	8
	SPOT 5	HRG PAN and MS	5 and 10	2003–2013	18
	IRS-1C/D	PAN	5.7	1997–2006	14
	RapidEye	REIS	6.5	2010–2019	11

account for misregistration in both the latitudinal and longitudinal directions. Uncertainty of the glacier length was then expressed as the maximum deviation among the two features from the mean position of each of them computed across all the orthoimages.

2.3.2 Surface velocity

We derived annual surface velocities with two different approaches based on image correlation: for 1996–2020, we processed single pairs of summer orthoimages (generated in Sect. 2.2); for 2017–2023, we produced annual mosaic combinations based on the dense Sentinel-2 archive.

The single summer orthoimages were manually selected for minimum snow and cloud cover on the glacier; the scenes are available for all years from 1996 to 2020, with gaps in 1999 and 2008–2009 (Table A1). We computed east/west and north/south displacements using the frequency correlator of geoCosiCorr3D, with a 128-pixel window size (Leprince et al., 2007; Aati et al., 2022). To increase coverage, we also correlated scenes from different sensors (SPOT with IRS; RapidEye with Pléiades), bilinearly resampling to 5 m

where needed. To improve correlation quality, we preprocessed the images with contrast limited adaptive histogram equalization (CLAHE; Pizer et al., 1987; Van Wyk De Vries and Wickert, 2021). We then applied common filters to the displacement maps (e.g., Heid and Kääb, 2012; Millan et al., 2019; Beaud et al., 2022): we discarded pixels of low signal-to-noise ratio (below 0.97), excessive velocity magnitude (above 200 m yr^{-1}; Fig. 4a), and small isolated specks (fewer than 100 contiguous cells). We also detected outliers with an 11×11-pixel moving-window median filter, thresholded at 2 standard deviations, and subtracted the median east/west and north/south displacements over stable terrain to account for residual misregistration. We finally extracted along-flow velocity profiles on the glacier tongue (Fig. 4b) and filtered out longitudinal strain rates above 0.1 yr^{-1} (e.g., Zheng et al., 2023), based on the values reported by Emelyianov et al. (1974) for the fast-flow episode of 1972–1973. Velocity derivation from SPOT and IRS was possible only on the lower tongue due to sensor saturation on snow-covered terrain. For each correlated pair, uncertainty was estimated as the normalized mean absolute difference (NMAD) of velocity measured over stable terrain (Scherler et al., 2008; Mil-

lan et al., 2019; Paul et al., 2022). The image pairs cover slightly inconsistent time intervals, with acquisitions ranging from 26 July to 15 September; a seasonal cycle in surface velocity could then introduce a bias in our annual results. This effect was accounted for by conservatively assuming velocity deviations of $\pm 50\%$ of the annual average over a number of days equal (for each pair) to the difference between 365 and the actual interval. The resulting uncertainty range was then quadratically summed with the NMAD (Fig. 4a).

Over 2017–2023, we derived surface flow velocities from the Sentinel-2 archive. Based on the cloud masks provided with each Sentinel-2 product, we discarded all acquisitions showing clouds on more than 10% of the glacier surface. We preprocessed the scenes with CLAHE followed by an orientation filter (Fitch et al., 2002; Van Wyk De Vries and Wickert, 2021); the latter further improved correlation between Sentinel-2 scenes, unlike for the 6 and 8 bit data from SPOT and IRS. We then ran the image pairs through the frequency correlator of geoCosiCorr3D separately within each of the two orbital tracks and four spectral bands (Sect. 2.1). For correlation, we included all pairs with time separations of 5 to 100 and 300 to 430 d, in order to minimize the variability of surface characteristics and solar illumination (Millan et al., 2019). We obtained approximately 68 000 displacement maps with a resolution of 40 m. The maps were filtered with the signal-to-noise ratio and magnitude thresholds as above, but (for computational performance) we omitted the other filters applied to single image pairs. Instead, after subtraction of stable-terrain residual displacements, the east/west and north/south velocity maps were stacked within each year, computing velocities for each pixel as the median of all available values. Results of the four bands were very similar (mean pixel-wise standard deviation of $1.1\,\text{m}\,\text{yr}^{-1}$ within the glacier outline) and were combined using the arithmetic average, weighted by the number of scene pairs contributing to each pixel. The final results were two sets of annual velocity maps – one per relative orbit – representative of surface velocity from one summer to the next. Note that Sentinel-2 products are disseminated with different processing baselines depending on acquisition date (European Space Agency, 2024). A noteworthy processing inconsistency is the use of different DEMs for orthorectification (Kääb et al., 2016): initially Planet DEM90, replaced by Copernicus GLO-90 in 2021 and Copernicus GLO-30 in 2023. Other relevant changes include the activation of geometric refinement using a global reference image for GCPs (since 2021) and a recalibration of the Sentinel-2B sensor radiometry to that of Sentinel-2A since 2022. As of early 2024, the full archive is undergoing backwards reprocessing to a common baseline, featuring all the improvements introduced over the years; thus, the more recent scenes are available in two versions. We verified the minor impact of such processing changes by running our pipeline twice: over the original baseline and over the reprocessed one. Considering all Abramov glacier cells faster than $10\,\text{m}\,\text{yr}^{-1}$ (cf. Fig. 4c/d),

the resulting absolute differences in surface velocity magnitude were within $5\,\text{m}\,\text{yr}^{-1}$ in more than 99% of all pixels. Hereafter, we retain the results obtained with reprocessed scenes whenever available.

2.3.3 Surface elevation and volume changes

We computed surface elevation changes from DEM differences. We implemented a uniform pipeline for the processing and analysis of all DEM pairs of interest, with time separations ranging from 5 d to more than 30 years. All grids were initially cropped to the Abramov glacier region and bilinearly resampled to a common projection (Universal Transverse Mercator zone 42N) and resolution (30 m, except for comparisons of the Pléiades high-resolution DEM pairs which were kept at the original 4 m). Then, the more recent DEM of the pair was coregistered to the older one using the approach in Nuth and Kääb (2011), followed by a 2D tilt correction (Girod et al., 2017) and the subtraction of residual median vertical offset over stable terrain. Such terrain was delimited by exclusion of (1) the RGI outlines, buffered by 200 m; (2) the slopes above 30° (Denzinger et al., 2021); and (3) all outlier cells whose absolute difference before coregistration was greater than four NMADs (Hugonnet et al., 2022). After coregistration, the DEM difference was first filtered (within the glacier outline) using simple thresholds on the absolute change. Based on long-term in situ observations (Suslov et al., 1980), we used conservative threshold values of 200 and 50 m for the lower tongue and upper region, respectively, separated at 4000 m a.s.l. (Fig. 1). Since the largest elevation changes occur far away from such a demarcation line (Fig. 5a, b, c, d), sensitivity to its chosen altitude is very low. As a second step, we quantified across- and along-track elevation biases (Hugonnet et al., 2022; Falaschi et al., 2023). We computed the along-track coordinate of each grid cell as follows:

$$x_{\text{al}} = -x \cdot \sin(\theta) + y \cdot \cos(\theta), \tag{1}$$

where x and y are the column and row numbers, respectively, of the cell and θ is the ground track of the satellite; the across-track coordinate is simply perpendicular and was expressed similarly. We then computed elevation differences on stable terrain and calculated the mean difference within 500 bins of the across-track/along-track coordinate. We corrected some common biases using polynomial or spline fits. Specifically, we compensated for the track biases of Pléiades as in Falaschi et al. (2023); we also mitigated KH-9 MC DEM artifacts from film scanning (Dehecq et al., 2020) and the residual artifacts of KH-4B and KH-9 PC using, in both cases, along-track spline fits. Following Nuth and Kääb (2011) and Gardelle et al. (2012), we also quantified (using the same method) biases related to maximum and minimum terrain curvature, absolute altitude, slope, and aspect; we simply verified that the mean magnitude of such biases did not exceed the spread observed for each bin, but no cor-

rection was applied to the grids. After a second coregistration of all the bias-corrected DEMs, we filtered the DEM differences using a threshold of 3 standard deviations within 100 m elevation bands (Berthier et al., 2004; Ghuffar et al., 2023). Then, the mean gap-filled elevation change was calculated using the local hypsometric method (McNabb et al., 2019). We considered regions of interest to be the entire glacier and some smaller polygons covering the tongue and terminus areas (Fig. 5). Finally, uncertainties in the elevation changes were estimated using the stable-terrain analysis in Hugonnet et al. (2022). We first calculated the dependence of DEM error on slope and maximum curvature and used this to compute standardized uncertainties and compile a map of pixel-wise elevation error for each DEM difference. Then, we modeled the variogram of elevation error with a double-range exponential function to compute the number of effective samples of elevation difference and finally the uncertainty of integrated elevation change (Hugonnet et al., 2022). Uncertainty estimates were validated using Monte Carlo spatial sampling with circular patches (Berthier et al., 2016; Miles et al., 2018; Hugonnet et al., 2022). In a few cases, we observed a slight underestimation of uncertainty from variogram modeling compared with the patches method. We accounted for such a discrepancy by fitting a small fraction of fully correlated variance (average: 1.0 %) to the variogram result until the two estimates matched (Mannerfelt et al., 2024). Following Berthier et al. (2014) and Dussaillant et al. (2018), a conservative factor of 5 was used to multiply uncertainty of elevation change over data gaps.

While our study is focused on remote sensing of ice dynamics, several of our DEMs present almost complete spatial coverage of the glacier, including the accumulation area. We used them to provide geodetic mass balance estimates for six subperiods between 1973 and 2022, assuming a mean glacier density of $850 \, \mathrm{kg \, m^{-3}}$ (Huss, 2013). Unlike for local ice thickness changes, for glacier-wide mass balance we only considered optical DEMs to avoid biases from radar penetration in the upper firn area (Barandun et al., 2015; Dehecq et al., 2016; Fan et al., 2023). Acquisition dates of the selected DEMs range from 12 July to 29 November, rendering it necessary to perform seasonality correction of geodetic volume changes (Cox and March, 2004; Cogley, 2009). This correction was computed by adding or subtracting the respective glacier-wide mass balance derived from the calibrated daily simulation in Kronenberg et al. (2022); correction values range from -0.03 to $+0.24 \, \mathrm{m \, w.e. \, yr^{-1}}$. We computed mass balance uncertainty following Dussaillant et al. (2018), using standard error propagation of the uncertainties of (1) integrated elevation change, including data gaps (Dussaillant et al., 2018; Hugonnet et al., 2022); (2) glacier area (5 %; Paul et al., 2013); (3) density conversion ($60 \, \mathrm{kg \, m^{-3}}$; Huss, 2013); and (4) seasonal correction ($0.7 \, \mathrm{m \, w.e. \, yr^{-1}}$; RMSE between modeled and measured mass balance in Kronenberg et al., 2022, which we linearly rescaled from 1 year to the actual number of days of the seasonal correction

for each subperiod). Uncertainty of density conversion over short periods is further discussed in Sect. 4.3.

We checked the consistency of our remote sensing data over three annual intervals (between 2003 and 2006) at the glacier terminus region by computing the ratio of depth-averaged to surface velocity via simultaneous estimation of volume changes, surface velocity, absolute ice thickness, and surface mass balance. This calculation is presented in Appendix D.

3 Results
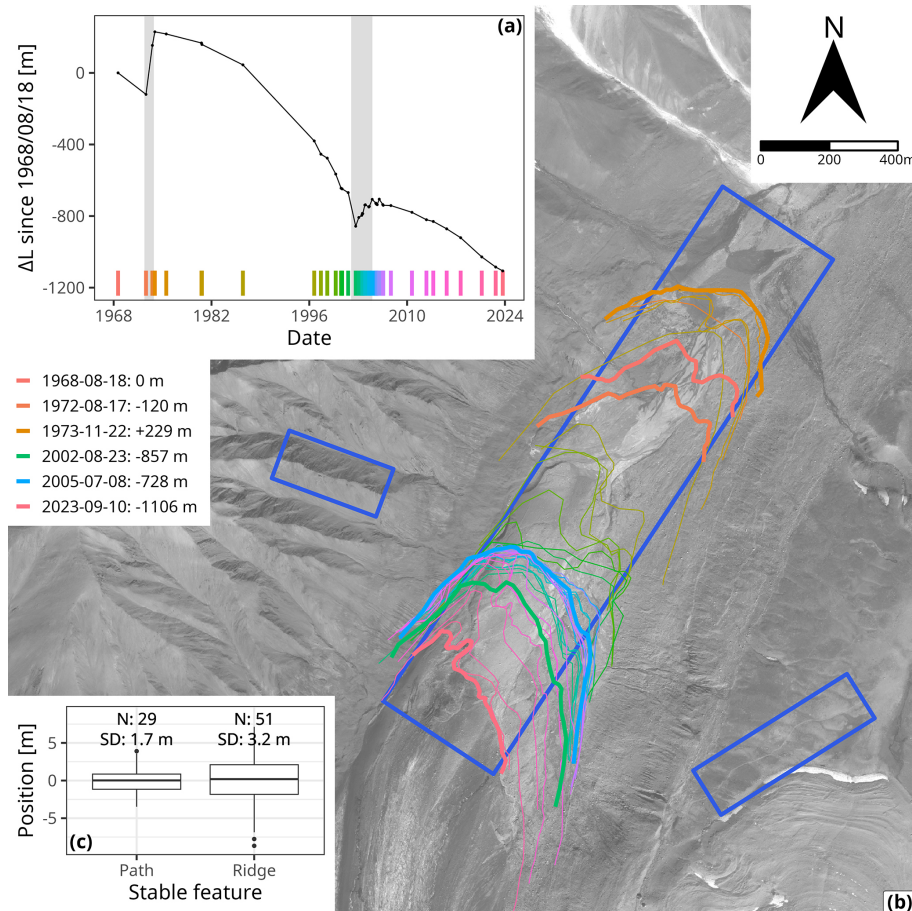
3.1 Glacier length changes

We obtained a set of 40 terminus positions and width-averaged length changes over 1968–2023 (Fig. 2). The time separation between consecutive measurements (Fig. 2a) ranges from 21 d (during the early 2000s) to 10 years (1986 to 1996). The terminus shows an overall trend of retreat over the 55 years, with a total change of $-1106 \pm 4 \, \mathrm{m}$ corresponding to a mean rate of $20.09 \pm 0.07 \, \mathrm{m \, yr^{-1}}$. This trend was interrupted by two sudden transitions to rapid terminus advance, in 1972 and 2002. The second advance was not observed in situ as this occurred just after the permanent monitoring program was discontinued. Total advance during the two events was $350 \pm 6 \, \mathrm{m}$ from August 1972 to November 1973 and $151 \pm 2 \, \mathrm{m}$ from August 2002 to January 2006. However, observation of the exact dates of minimum and maximum length could be missing from our dataset. We derived maximum advance rates of $82.3 \pm 0.3 \, \mathrm{cm \, d^{-1}}$ in 1972–1973 and $44.3 \pm 0.8 \, \mathrm{cm \, d^{-1}}$ in summer 2003. Seasonal oscillations of 30–50 m are visible during the more recent event, with an alternating pattern of marked advance during the cold season and smaller retreat in summer. Both advances were followed by an initially slow but gradually accelerating front retreat. Length uncertainties from the digitized stable features are always within $\pm 10 \, \mathrm{m}$, with standard deviations of 1.7 and 3.2 m for the unpaved road and the ridge, respectively (Fig. 2c). In particular, the errors of length estimated on all scenes at 5 m resolution (the largest group in our dataset) are within $\pm 5 \, \mathrm{m}$ in 49 out of 51 cases, corroborating the rule of thumb of ± 1 pixel proposed by Paul et al. (2013).

3.2 Surface velocity

Glacier velocities are shown in Fig. 3 for transverse profile 4 of the historical monitoring network (Fig. 1). The profile is located about 2.2 km upstream of the 2023 terminus and presents the most complete results in our dataset. Velocity peaks are visible in 1972–1973 and in the early 2000s, corresponding to the phases of terminus advance. The time series shows a marked acceleration occurring just before and in the early stages of the 2000s advance: mean annual velocity increased regularly between 1996–1997 and 2002–2003, almost doubling from 57 to 106 $\mathrm{m \, yr^{-1}}$. Afterwards, a faster –

Figure 2. (a) Length changes of Abramov glacier according to the rectilinear box method. Zero reference is 18 August 1968. Marks at the bottom match the date and color of the outlines in panel **(b)**. Gray shading indicates the period of the two pulsations. The six listed dates (with their cumulative length changes) correspond to the extreme positions of the two pulsations and the earliest and latest points in our dataset; the respective outlines are shown in bold in panel **(b)**. **(b)** Digitized termini of Abramov glacier from 1968 to 2023. Blue rectangles correspond to the rectilinear boxes used to calculate length changes of the glacier and the stable features. Background: Pléiades © CNES 2023, Distribution AIRBUS DS. **(c)** Box plots of relative deviations of the stable feature positions from their mean.

yet gradual – slowdown is visible, continuing at least into 2006–2007. Minimum velocity was probably reached between 2007 and 2010; since then, a new slow regular acceleration has occurred, leading again to a doubling in velocity by 2023 (from 17 to 37 m yr^{-1}). Velocity changes at other transverse profiles of the historical monitoring network are qualitatively similar, but with more data gaps. The strong multiannual velocity variations did not reflect corresponding changes in ice thickness (Fig. 3): at profile 4, the latter remained constant (within uncertainty) during the early 2000s, and it has gradually lost 18 ± 4 m (10 %) since 2011. We found some specific differences between the early 2000s and the previous speedup event of 1972–1973: our results show a progressive acceleration leading to a moderate velocity peak (108 ± 2 m yr^{-1}; about half the 1973 value) sustained between 2000 and 2003 and a gradual slowdown in subsequent years; by contrast, in situ observations of the early 1970s recorded a faster speedup (with a 5-fold increase

in the 2 years before the peak), a shorter duration of maximum velocities (about 1 year), and an especially abrupt termination, occurring within less than 10 months (Suslov et al., 1980). Minimum velocities also appear to be lower after the first event, although values for 2007–2010 are missing from our dataset.

Longitudinal velocity profiles over 1996–2007 (Fig. 4a) show uniform acceleration and slowdown over the entire glacier tongue; only the first profiles are slower towards the terminus, confirming the presence of stagnant ice which, by 2000–2001, was being reached and overrun by the active front. The more recent velocity profiles (Fig. 4c, d) extend into the right branch and accumulation area thanks to the superior radiometric specification of Sentinel-2 MSI compared with that of older sensors. We observe acceleration since 2017–2018 to be again quite uniform along the glacier; however, on the right branch, it is visible only downstream of the icefall at 4150 m a.s.l. (Figs. 1, 4b, d). Flow velocities appear
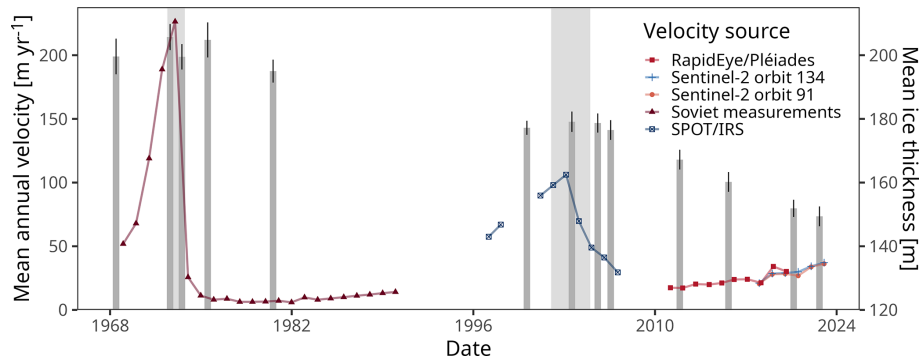
Figure 3. Mean annual ice surface velocity at transverse profile 4 (Fig. 1). Soviet measurements are from Glazirin' et al. (1993). Gray bars show DEM-derived mean ice thickness at the same profile. Error intervals reflect only uncertainty from the surface DEMs; uncertainty in bed elevation – which affects all thickness values equally – is not included. Gray shading indicates the period of the two pulsations.

to have peaked by 2022–2023, when a slight reduction of $2\,\mathrm{m\,yr^{-1}}$ is visible over the upper-left branch compared with the previous year. Conversely, values on the lower tongue still increased by about the same amount over 2023, suggesting a down-glacier propagation of the wave of maximum velocity. In the full map of glacier surface velocity (Fig. 4b), the different flow regions are visible and match the boundaries defined by medial moraines (Fig. 1). The slower flow of small nearby glaciers is also resolved.

Computed uncertainties of single-pair surface velocities (Fig. 4a) are $4.3\,\mathrm{m\,yr^{-1}}$ on average but as low as $0.6\,\mathrm{m\,yr^{-1}}$ for 2005–2006. In the annual Sentinel-2 mosaics, NMAD over stable terrain (defined as in Sect. 2.3.3) is always between 0.5 and $1.5\,\mathrm{m\,yr^{-1}}$. Over 2017–2020, the RMSE between Sentinel-2 mosaics and single annual correlations is $3.5\,\mathrm{m\,yr^{-1}}$ at transverse profile 4 (Fig. 3). The plausibility and significance of such estimates are discussed in Sect. 4.3.

3.3 Surface elevation and volume changes

3.3.1 Thickness patterns

Our DEM differences follow the evolution of the glacier surface over the course of both pulsations mentioned above (Fig. 5). During the active phases (1972–1973 and 2000–2003; Fig. 5a, b), ice thickness significantly increased at the terminus, with mean (maximum) changes of 29 ± 4 $(90 \pm 5)\,\mathrm{m}$ in the first phase and 9.1 ± 0.6 $(39 \pm 4)\,\mathrm{m}$ in the second one. Within the same periods, a modest – albeit widespread – thinning is visible over an upstream reservoir region, with a mean (maximum) decrease of 10 ± 4 $(20 \pm 5)\,\mathrm{m}$ in the 1970s event and 2.8 ± 0.5 $(10 \pm 3)\,\mathrm{m}$ in the 2000s one. Such a spatial pattern was reversed during the quiescent phases (Fig. 5c, d), when the lower tongue lost a mean (maximum) of 24.2 ± 1.1 $(104 \pm 4)\,\mathrm{m}$ and 19.6 ± 0.2 $(76 \pm 2)\,\mathrm{m}$ of ice thickness over 1980–2000 and 2003–2020, respectively. Meanwhile, the accumulation area gained a mean (maximum) of 1.5 ± 1.2 $(14 \pm 4)\,\mathrm{m}$ and 2.0 ± 0.4 $(12 \pm 2)\,\mathrm{m}$, respectively, during these two periods of time,

despite a consistent trend of overall mass loss on the whole glacier (Barandun et al., 2015; Denzinger et al., 2021). When considering only the terminus region (the lowest $0.6\,\mathrm{km^2}$ before front advance, as delimited by Emelyianov et al., 1974), ice volume almost doubled during both active phases (Fig. 5g, h), and mean thickness over the same region increased in the 1970s from 57 to $121\,\mathrm{m}$ and in the 2000s from 38 to $67\,\mathrm{m}$. Absolute values were larger in the 1970s; given that the advance covered a longer distance (Fig. 2), the considered terminus region (Sect. 2.3.3) is located further upstream from the snout than that in the early 2000s (Fig. 5a, b). Some subseasonal trends are also captured in Fig. 5f and h: downstream mass transfer in the summer of 2003 was stronger than ice ablation, leading to a volume increase during August, while the opposite is true for the year 2005. Ice thickness changes derived from SPOT 5 HRS closely match the ASTER results at corresponding dates, over both the terminus region and the broader tongue below transverse profile 4 (Fig. 5f, h). Uncertainties are generally smaller in HRS DEMs than in ASTER, reflecting the higher spatial resolution of the original data. Calculations on HRS DEM pairs over 5 d intervals (Sect. 2.2.2) yielded mean elevation changes between -0.5 ± 3.0 and $0.1 \pm 1.6\,\mathrm{m}$ over $67.5\,\mathrm{km^2}$ of RGI polygons, confirming the stability of our results. The distribution of standardized elevation differences is very similar and close to Gaussian both on-glacier and off-glacier (Fig. C1).

3.3.2 Geodetic mass balance

Geodetic mass balance results are presented in Table 3 and Fig. 6a for six time intervals between 1973 and 2022. All periods were characterized by mass loss; the most negative mass balances correspond to the years immediately following the 1972–1973 pulsation and to the period 2020–2022. This last period displays exceptional thinning over the entire glacier extent up to the highest elevations (Fig. 6b). By
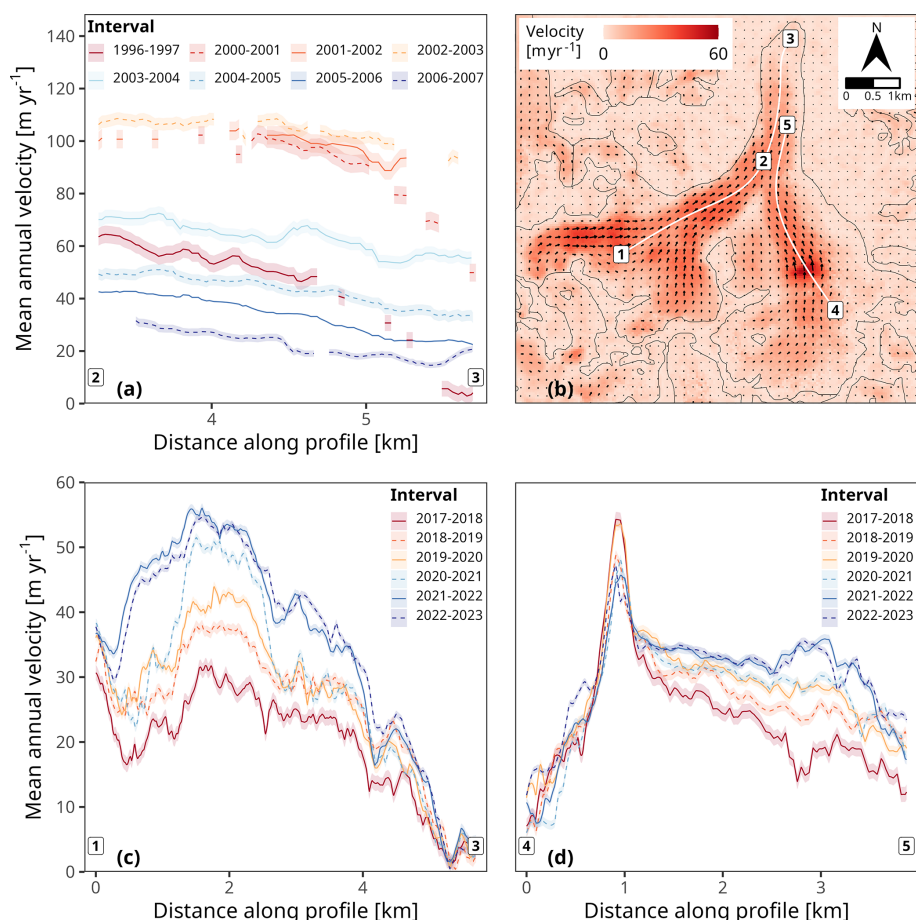
Figure 4. Longitudinal profiles of mean annual ice surface velocity from **(a)** SPOT and IRS single pairs, lower tongue; **(c)** Sentinel-2 orbit 91 mosaic, left branch and lower tongue; and **(d)** Sentinel-2 orbit 91 mosaic, right branch. **(b)** Mean 2017/18 velocity from Sentinel-2 orbit 91 mosaic; white profiles and locations 1 to 5 correspond to panels **(a)**, **(c)**, and **(d)**. Uncertainty shading reflects the residual velocity of stable terrain (Sect. 4.3).

contrast, we found a mass budget close to balanced between 1980 and 2003, concurrent with a front retreat of 950 m.

4 Discussion

4.1 Glacier dynamics

The compiled datasets provide information on Abramov glacier dynamics at high spatial and temporal resolution over 55 years. In particular, frequent scene availability in the late 1990s and early 2000s enables reconstruction of glacier evolution during the period of interrupted in situ monitoring, including an unobserved phase of fast ice flow. Over more than 5 decades, we found no positively correlated relationship between trends of ice thickness and velocity (Fig. 3). Rather, ice thickness patterns in 1972–1973 and 2000–2003 (Fig. 5) provide evidence of rapid mass redistribution from an upper reservoir to the lower tongue, followed by longer periods of recovery in which surface height trends are in-

verted. These results indicate unstable flow conditions typical of surge-type glaciers (e.g., Raymond, 1987; Round et al., 2017; Benn et al., 2019), challenging the representativity of Abramov as reference for mass balance. Still, the whole region features a high density of surge-type glaciers (Glazirin' and Shchetinnikov, 1980; Goerlich et al., 2020; Guillet et al., 2022), which could put into question the representativity of even a stable glacier towards regional extrapolation of the observed trends of mass balance.

The heterogeneous character of the two pulsations (Sect. 3.2) suggests long-term evolution of the mechanisms behind accelerated flow. The low and declining intensity of active phases could denote a progressive transition away from the unsteady flow regime and towards more stable conditions, possibly as a result of multidecadal negative mass balance (Hoinkes, 1969; Dowdeswell et al., 1995; Denzinger et al., 2021). Enhanced ablation of the reservoir area in the most recent years (Fig. 6b) is expected to further reduce mass buildup, depriving the glacier of enough ice to be transferred downstream in a surge (e.g., Flowers et al., 2011). However,
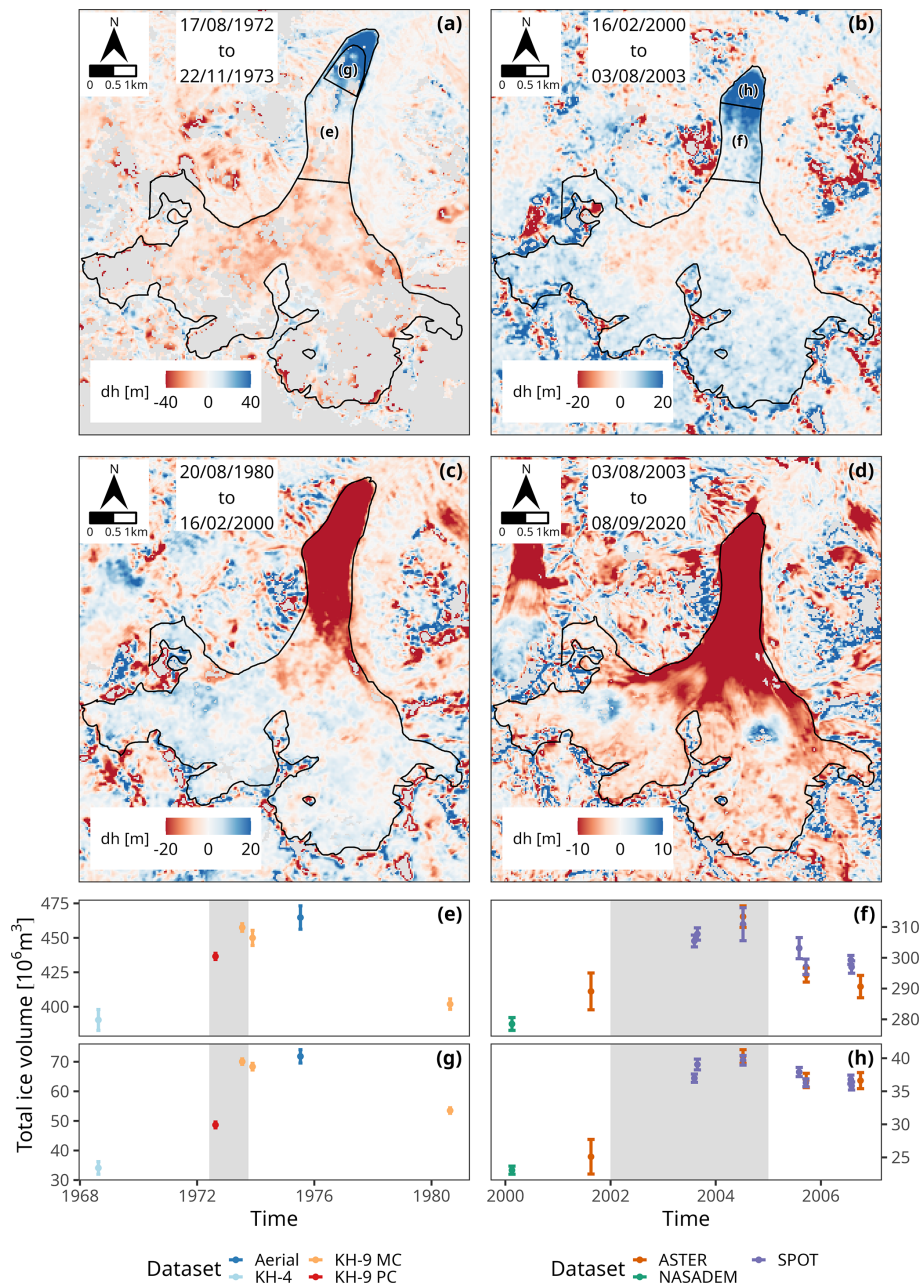
Figure 5. Abramov glacier thickness and volume changes. **(a, b, c, d)** DEM differences during two surge cycles. **(a)** Active phase of 1972–1973. **(c)** Quiescence over 1980–2000. **(b)** Active phase of 2000–2003. **(d)** Quiescence over 2003–2020. Color scale ranges are limited to preserve detail in the regions of slower change. Letter-marked polygons correspond to the ice volume time series of panels **(e)**, **(f)**, **(g)**, and **(h)**. **(e, g)** Evolution of total ice volume over **(e)** the tongue below profile 4 and **(g)** the terminus region, from 1968 to 1980. Gray shading indicates the period of the 1972–1973 pulsation. Panels **(f)** and **(h)** are as panels **(e)** and **(g)** but from 2000 to 2006. Gray shading indicates the period of the early 2000s pulsation. Boundaries of the regions are shown in panels **(a)** and **(b)**. Error bars reflect only the uncertainty of surface DEMs and not the bed elevation uncertainty, which systematically affects all values by the same amount.

we also found the possible attainment of a new modest velocity peak by 2022–2023 (Fig. 4c, d), about 20 years after the previous one. If confirmed, a shorter duration of the quiescent phase (compared with the 30 years for the first observed one) would be consistent with a long-term increase of net

annual accumulation rates (Dowdeswell et al., 1995; Eisen et al., 2001; Copland et al., 2011), which was quantified at about 50 % between 1970–1997 and 2011–2018 in the upper accumulation area (Kronenberg et al., 2021). Further interpretation of dynamic instability at Abramov should involve

Table 3. Geodetic mass balance of Abramov glacier, including seasonality correction. Uncertainty ranges are discussed in Sect. 4.3. Reference initial volume (1973) is 2.55 km³.

Date	Specific annual mass balance [m w.e. yr⁻¹]	Cumulative volume loss [%]	Volume loss rate [% yr⁻¹]
1973			
	-0.89 ± 0.44	5.6	0.80
1980			
	-0.10 ± 0.05	7.5	0.08
2003			
	-0.27 ± 0.09	9.4	0.23
2011			
	-0.50 ± 0.15	11.1	0.42
2015			
	-0.39 ± 0.05	12.7	0.33
2020			
	-1.05 ± 0.10	14.5	0.88
2022			

ice flow modeling and an examination of glacier dynamics at the mountain range scale.

4.2 Comparison with in situ observations and past studies

Historical variations of glacier length, thickness, and velocity until the 1990s have been described in numerous Soviet and Russian publications based on in situ measurements (Emelyianov et al., 1974; Abulkhasanova et al., 1979; Suslov et al., 1980; Dolgoushin and Osipova, 1982; Bassin and Kamnyansky, 1987; Glazirin' et al., 1993). A major goal of our study is to extend these time series, bridging the gap in the observations. However, rigorous quantitative comparison with our results is not straightforward due to several factors. First, spatial delimitation and aggregation of measurements is not always clear in the cited publications as, apparently, reported length changes often refer to the lowest point of the glacier and not to width averages as in our results, and whether stagnant debris-covered ice is considered part of the glacier or not remains unknown. The definition of "terminus region" and "glacier tongue" is also sometimes vague and inconsistent across authors. Second, reported time intervals of the changes are often imprecise, usually omitting the day specification – introducing a potential location mismatch by several tens of meters during episodes of fast flow. Third, even well-specified time intervals do not exactly match the available dates of our scenes. Fourth, we find considerable disagreement in the numbers reported by different sources, even in relation to a single a priori well-defined variable such as total advance of the glacier snout over the early 1970s: 420 m (Emelyianov et al., 1974), 500 m (Abulkhasanova et al., 1979), 401 m (Suslov et al., 1980), 625 m (Dolgoushin and Osipova, 1982), and 400 m (Bassin and Kamnyansky, 1987).
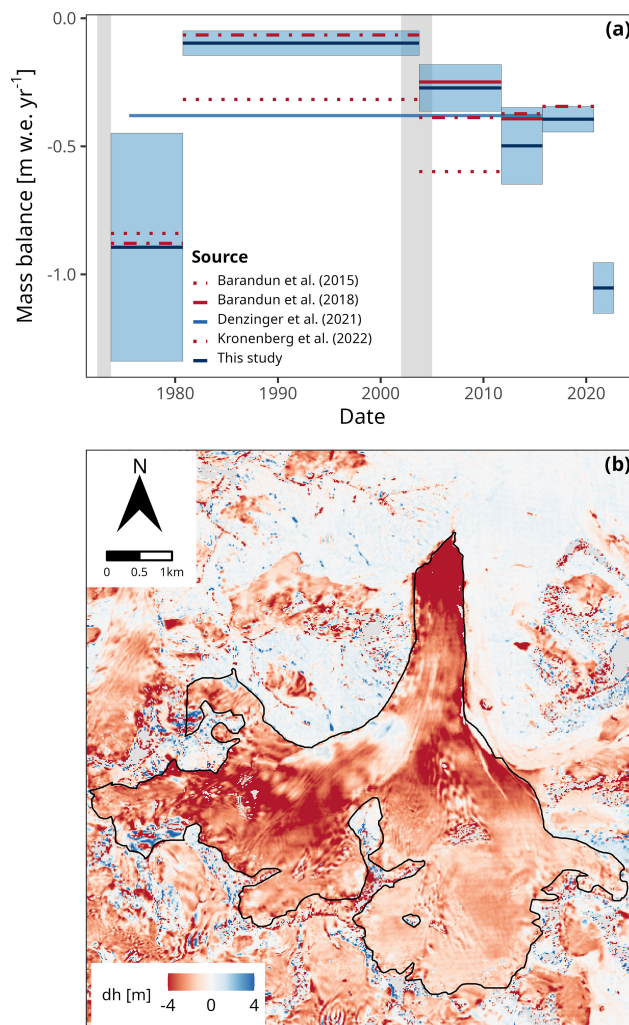
Figure 6. (a) Specific annual mass balance of Abramov glacier from our DEM differences and from previous studies; for readability, uncertainty is shown only for our results. Gray shading indicates the period of the two pulsations. **(b)** Pléiades DEM difference between 8 September 2020 and 5 September 2022.

Thus, comparisons against our remote sensing measurements – including front variations and ice volume changes – are potentially affected by inconsistent reporting of the in situ values.

For glacier length, our results (Fig. 2) indicate a progression of 350 ± 6 m between 17 August 1972 and 22 November 1973, when the terminus had already reached the maximum extent within a few meters. Combined with an in situ observation of advance of 82 m from September 1971 to November 1972 (Suslov et al., 1980), our observations support the lower values (about 400 m) among the range of Soviet estimates of total advance presented above. A recent reconstruction of Abramov glacier terminus positions was presented by Mandychev et al. (2017), also based on remote sensing and topographic data. It has no overlap with our
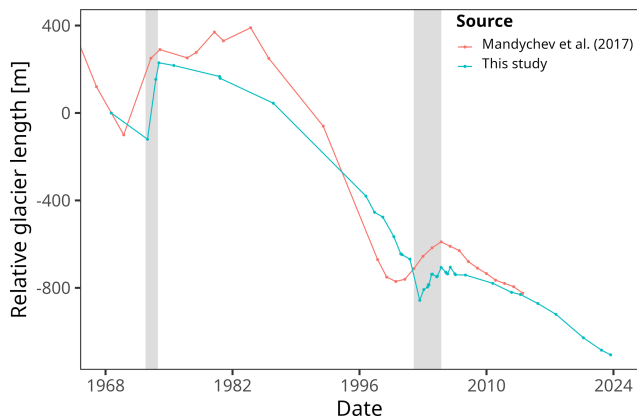
Figure 7. Length change of Abramov glacier from Mandychev et al. (2017) and from our study. Gray shading indicates the period of the two pulsations.

datasets: the study used the Landsat archive, some unrectified aerial frames which were not available to us, and several schematic maps of the glacier margin digitized from Soviet publications. The comparison (Fig. 7) shows a qualitative agreement of the overall trends of retreat and pulsations, but also several differences, likely related to both residual image distortions and lower scene resolution within that study. In several periods, the glacier is incorrectly classified as advancing – 6 years between 1977 and 1984, up to a 1978–1980 rate of $46.5\,\mathrm{m\,yr^{-1}}$. We find these results to be implausible, as they would lead to a terminus position 100 m forward in 1984 compared with the maximum of 1975 – in contrast with both the observed terminal moraine position and the very low ice velocity during the period (Fig. 3). During the more recent pulsation, Mandychev et al. (2017) report terminus advance starting in 2000 instead of 2002. This is apparently based on the omission of debris-covered ice at the terminus, visible on our SPOT and IRS images but not on lower-resolution Landsat scenes.

With the caveats mentioned above, we compare our estimates of ice thickness and volume changes against the in situ observations of the 1970s. For the net ice volume transferred to the tongue over 1972–1973, Suslov et al. (1980) report a value of $23.12 \times 10^6\,\mathrm{m^3}$, calculated from measurements of ice velocity and transverse cross-section (at profile 4) and surface ablation (downstream of profile 4). The DEM difference from KH-9 PC and MC (Fig. 5a) yields a total change of $32 \pm 10 \times 10^6\,\mathrm{m^3}$ over the same region between 17 August 1972 and 22 August 1973. Our measurement includes the whole period of fastest flow but misses the ice ablation of early summer of 1972. For the $0.6\,\mathrm{km^2}$ region of interest covering the terminus (Fig. 5a), Emelyianov et al. (1974) report a doubling of the total ice volume over the first 8 months of 1973. The value is slightly larger than the roughly 60 % change that we obtain in Fig. 5g but within the error range when factoring in the uncertainty of glacier bed

elevation (conservatively $\pm 20\,\%$ of the ice thickness, based on literature values: Grab et al., 2021). Due to systematically incomplete coverage of our DEMs in the accumulation area, we cannot quantify the total mass transferred away from the reservoir area over the early 1970s surge. However, our estimated thinning by up to $20 \pm 5\,\mathrm{m}$ (Fig. 5a) is very close to the values reported for the firn area cross-profiles in Suslov et al. (1980) (16.5 m) and on the map in Kotlyakov (1997) (20 m). Thus, we conclude that our estimates corroborate in situ measurements within the respective uncertainty ranges, despite the lack of rigorous comparison.

For mass balance (Fig. 6a), our results generally agree well with past estimates. Our results match within uncertainty the geodetic mass changes calculated over 1975–2015 by Denzinger et al. (2021) from structure-from-motion (SfM) and Pléiades data. Geodetic mass balance including two SPOT DEMs from 2003 and 2011 was also presented by Barandun et al. (2018) as validation of a daily mass balance model: our value for that period is predictably very similar (within $0.1\,\mathrm{m\,w.e.\,yr^{-1}}$), but we obtain a DEM with more complete coverage (97 % vs. 74 %). The mean geodetic mass balance computed for 1973–1980 (Table 3) matches historical glaciological estimates within $0.1\,\mathrm{m\,w.e.\,yr^{-1}}$ (Glazirin' et al., 1993; Pertziger, 1996; Kamnyansky, 2001). More recent periods can be compared against the calibrated model reanalyses of Barandun et al. (2015), Barandun et al. (2018), and Kronenberg et al. (2022). Our results generally support the findings of the full energy-balance simulation in Kronenberg et al. (2022), except over 2003–2011, where glaciological calibration data are missing. For that period, the temperature-index approach in Barandun et al. (2018) – which is constrained by transient snow line elevation from Landsat – provides the most comparable results.

Additional comparisons with remote sensing studies covering Abramov glacier are provided in Sect. 4.4. In particular, the active phase of the early 2000s is not well resolved by Landsat or ASTER, with regard to both ice movement on the tongue (Fig. E1a) and ice thickness trends at the terminus (Fig. E2).

4.3 Measurement uncertainties

Throughout the present study we quantify uncertainties with common methods mostly based on the analysis of stable terrain in the glacier vicinity. Comparison with in situ measurements from the 1970s indicates reasonable estimates for our observations and their uncertainties (Sect. 4.2). Still, lack of ground validation over the early 2000s is a significant limitation. In the following, we discuss some sources of uncertainty affecting our results.

The interpretation of glacier margins under debris or snow cover can introduce major errors in estimated glacier area and length changes (Paul et al., 2013, 2017, 2020). However, the achieved high temporal frequency of orthoimages and concurrent DEM differences allows close tracking of surface

height and morphology changes, enabling a consistent interpretation of glacier extents (e.g., Racoviteanu et al., 2009; Paul et al., 2020).

Our estimates of ice velocity uncertainty (Fig. 4a) mostly reflect the residual geometric inaccuracies within image pairs; still, error sources specifically affecting ice velocities are not that easily accounted for (e.g., Altena et al., 2022; Zheng et al., 2023). In particular, more frequent and severe mismatches are observed on-glacier, due to repeat formation of self-similar features such as ogives, crevasses, seracs, and avalanche deposits (Paul et al., 2015). Also, the melting surface can lead to more decorrelation and a different noise distribution compared with stable terrain (Millan et al., 2019; Zheng et al., 2023). Indeed, noise along the profiles in Fig. 4c and d is visibly larger than our NMAD estimate of 0.5 to 1.5 m yr^{-1} (Sect. 3.2). We also notice the potential impact of seasonal velocity changes on the Sentinel-2 velocity mosaics: the contributing image pairs (and thus the covered time intervals) are in principle different at each location, potentially leading to biases depending on the relative representation of the various seasons. A better characterization of uncertainties would require ground-based long-term measurement of annual and seasonal velocities. In one comparison with GPS over the Mont Blanc region, Millan et al. (2019) found annual discrepancies of Sentinel-2 mosaics of 4–6 m yr^{-1} for glaciers of width and velocity similar to those of Abramov.

The statistical framework of Hugonnet et al. (2022) allows uncertainty quantification in DEM differences from stable terrain, including the effects of heteroscedasticity and spatial correlation. Here, we also validate the results with the empirical spatial sampling in Berthier et al. (2016) and Miles et al. (2018). Still, our thickness change results over 1980–2000 and 2000–2003 (Fig. 5c, b) involve NASADEM heights affected by C-band radar penetration of dry snow and ice, which can lead to systematic uncertainties (especially in upper accumulation areas) which may not be fully represented on stable terrain (Gardelle et al., 2012; Barandun et al., 2015). Correction of the possibly underestimated glacier surface height for 2000 is not straightforward. In general, we would expect an intensification of the patterns of firn area thickening over 1980–2000 and thinning in the later period – magnitude of surge-like patterns is possibly underestimated by the use of NASADEM. For simplicity, here we assume that radar penetration involves just the layer of seasonal snow, returning the height of the (mostly thinly debris-covered) summer glacier surface (Buckley et al., 2023). Such an assumption probably becomes inadequate over the upper reaches of the accumulation area, well above our regions of interest (Bannwart et al., 2024). The magnitude of observed thickness change patterns (Sect. 3.3.1) exceeds the expected C-band penetration by a factor of 2 or more (Li et al., 2021; Fan et al., 2023).

For geodetic mass balance, the error budget is in most cases dominated by surface height change uncertainty; over

1973–1980, this is especially large (Fig. 6a) as a result of numerous data gaps in the accumulation area (Sect. 2.3.3). Of all DEM differences, the 2020–2022 Pléiades map (Fig. 6b) is the most accurate, with an aggregated error of just ±0.1 m over the Abramov outline and almost no gaps or seasonal mismatch. Glaciological mass balance is in excellent agreement, with a 2020–2022 mean value of −1.03 m w.e. yr^{-1} (World Glacier Monitoring Service (WGMS), 2024). However, the short observation interval renders density conversion highly uncertain, and the 60 kg m^{-3} error assumption probably becomes inadequate (Huss, 2013). In particular, exceptional thinning above the firn line could be buffered by firn density increase at depth due to enhanced meltwater refreezing, leading to a more positive internal mass balance and thus systematic overestimation of mass loss (Kronenberg et al., 2022; Berthier et al., 2023). Still, Abramov glacier has a mostly temperate firn area with decreasing pore space over the last few decades (Kislov et al., 1977; Kronenberg et al., 2022), thus limiting the potential for meltwater refreezing. A conservative lower bound for the total change can be computed assuming zero balance over the 8 km^2 of snow- and firn-covered area. The result (−0.80 m w.e. yr^{-1}) is still exceptionally negative compared with that in all subperiods since 1980.

4.4 Evaluation of datasets and methods

Declassified satellite scenes have been increasingly used to assess historical glacier evolution since the 1960s to 1980s, both at regional to global scales (e.g., Pieczonka and Bolch, 2015; Maurer et al., 2019; Zhou et al., 2019; Dehecq et al., 2020; Bhattacharya et al., 2021) and for individual catchments and large glaciers (e.g., Bolch et al., 2011, 2017; Goerlich et al., 2017; Ghuffar et al., 2023). However, these studies usually lack ground validation during the early periods, especially for the data-scarce Central Asia region. In the present work we observe that length and volume changes from KH-4 and KH-9 are consistent with in situ measurements over one surge cycle of the relatively small Abramov glacier. Moreover, accuracy derived from stable terrain is similar to a 1975 SfM DEM obtained from a dedicated aerial survey (Fig. 5e, g).

From the SPOT, IRS, and RapidEye archives we assembled a dataset of late-summer imagery at 5 m, mostly complete at annual frequency between the mid-1990s and the late 2010s. Our time series successfully bridges the gap in ice dynamics observations at Abramov. In fact, the covered time span is of particular interest for all reference glaciers in Central Asia, whose monitoring was interrupted following the Soviet Union collapse, and for sites which have been newly established over the last few years and lack detailed historical observations, for example, in Tajikistan (Barandun et al., 2020). Within our dataset we find an especially dense scene availability during the early 2000s (Table 2; Fig. 2b). Between 2000 and 2005, we observe more than twice as many

cloud-free summer scenes than from Landsat and ASTER combined, owing to irregular acquisitions by the latter platforms over their initial period of operation. Thus, SPOT and IRS have the potential to become a primary data source to reconstruct glacier change over those years.

Beside scene availability, the higher spatial resolution unlocks details of ice dynamics which are poorly resolved on Landsat and ASTER (Figs. 5, 7; Appendix E). Indeed, dynamics of smaller and slower-flowing glaciers are beyond the reach of optical remote sensing from such sensors (Paul et al., 2022). A notable consequence is that most inventories of surge-type glaciers can be biased towards larger entities (Goerlich et al., 2020). Higher-resolution imagery can support the assessment of unstable flow at the smaller ice bodies.

To derive ice velocities, we performed several mixed correlations involving scenes from different sensors (SPOT with IRS, RapidEye with Pléiades; Table A1). To the best of our knowledge, such a multi-sensor correlation has not been previously applied to glaciers. Thanks to full control over the orthorectification process (unlike with Landsat and Sentinel), the resulting displacement maps show limited residual distortions (Fig. 4a).

Several studies have used different spectral bands of Sentinel-2 to derive glacier surface displacements (Altena and Leinss, 2022). Results from the various bands usually match within uncertainty ranges, indicating adequate inter-band registration and calibration (Lacroix et al., 2018; Altena et al., 2022). Still, in our four-band composites, we notice a small noise reduction in the upper accumulation area compared with velocities derived from a single band; we observe virtually no change on the glacier tongue.

We compared our results at Abramov glacier with several published remote sensing studies, providing ice velocity and surface height changes at a global scale. While some features of the glacier dynamics are recognizable within the latter (Fig. 5f, h), our results provide better detail and accuracy than existing datasets. For annual surface velocity, we evaluated the velocities of ITS_LIVE, which covers 1985–2022 from Landsat 4–8 (Gardner et al., 2018, 2024), as well as the 2014–2021 Sentinel-1 grids of Friedl et al. (2021) and the 2017/18 biannual result of Millan et al. (2022), based on Sentinel-1, Sentinel-2, and Landsat 8. The coarse grids of ITS_LIVE and Friedl et al. (2021) (at 240 and 200 m resolution, respectively) do not capture most of the surface displacement over the lower tongue (Fig. E1b, c). Note that no velocity change is recognizable during the active phase of 2000–2003 (Fig. E1a). The result in Millan et al. (2022) is more detailed but includes several patches of outlier values and stronger noise in the flow direction (Figs. E1d, 4b). For ice thickness patterns, we examined the 5-year grids of the surface height change rate in Hugonnet et al. (2021), calculated at 100 m resolution from ASTER stereo pairs via Gaussian process regression (Fig. E2). We found that no ice thickening at the terminus is visible over 2000–2005, which would

prevent an automated identification of the active phase from the dataset.

Overall, the methods used throughout the study are mainly based on open-source tools. Most steps do not require manual intervention, except for (1) cloud-free image selection (for which some automated approaches already exist: e.g., Fisher, 2014), (2) front digitization, and (3) manual picking of initial GCPs (in case an appropriate reference orthoimage is not already available for their automated detection). For GCPs-based orthorectification, we consider the availability of a high-resolution reference such as Pléiades not mandatory: a cloud-free scene from Sentinel-2 can be used instead. Thus, application at a larger scale could be relatively efficient to derive time series of regional-scale velocity and thickness changes for the early 2000s.

5 Conclusions

In the present study we compile a 1968–2023 dataset of high-resolution orthoimages and DEMs at Abramov glacier by processing raw optical scenes from multiple archives. Our reconstruction allows studying the long-term evolution of unstable ice dynamics, revealing two cycles of mass redistribution typical of surge-type glaciers. During quiescence, we found a sustained gradual acceleration – quite uniform over the glacier tongue. The observed phases of fast flow show decreasing intensity and increasing duration, possibly suggestive of a multidecadal transition towards more stable dynamics. We also note the potential attainment of a third modest peak of ice velocity by 2023.

Our observations are in good agreement with results from historical and modern research at the site. We find that length and volume estimates from declassified reconnaissance satellites are consistent with in situ measurements. The 5 m scenes of IRS, SPOT, and RapidEye extend the observational time series of ice dynamics at Abramov, bridging the 12-year gap of interrupted monitoring. In particular, they allow quantification at the subseasonal scale of the second unobserved active phase, which is poorly resolved by Landsat and ASTER products. The 1973–2022 geodetic mass balances over six subperiods support the negative estimates of recent model-based studies.

Our methods can be expanded to a larger scale efficiently to investigate regional evolution of glacier velocity over the past 2 decades. Such work would extend early studies on the distribution of unstable ice flow in the Pamir-Alay (Glazirin' and Shchetinnikov, 1980; Glazirin' et al., 1987). Compared with the Landsat record, we anticipate a better coverage of ice dynamics, especially on smaller and slower-moving entities, supporting compilation of more complete inventories of surge-type glaciers. At Abramov glacier, further interpretation of the observed dynamics should involve ice flow modeling, constrained by the velocity and volume changes derived within our study. Of particular interest would be the relation-

ship between the observed unstable flow dynamics and the well-known mass balance of this reference glacier.

Appendix A: Lists of satellite scenes

Here, we provide the list (Table A1) of orthoimages used for surface velocity derivation (Fig. 3) and the list (Table A2) of processed declassified scenes from reconnaissance satellites.

Table A1. Orthoimages at 5 m resolution used for single-pair annual surface velocity derivation.

Date (dd/mm/yyyy)	Platform	Notes
15/09/1996	SPOT 3	PAN, resampled from 10 m
30/08/1997	IRS-1C	PAN
28/07/1998	IRS-1D	PAN
02/09/2000	IRS-1C	PAN
02/09/2001	IRS-1C	PAN
23/08/2002	IRS-1C	PAN
27/08/2003	SPOT 5	PAN
12/08/2004	IRS-1C	PAN
03/08/2005	SPOT 5	PAN
02/08/2006	SPOT 5	PAN
06/09/2007	SPOT 5	PAN
11/09/2010	RapidEye	Band 2
08/09/2011	RapidEye	Band 2
01/08/2012	RapidEye	Band 2
07/09/2013	RapidEye	Band 2
02/09/2014	RapidEye	Band 2
20/08/2015	Pléiades	PAN, resampled from 0.5 m
27/07/2016	RapidEye	Band 2
31/08/2017	RapidEye	Band 2
05/09/2018	RapidEye	Band 2
26/07/2019	RapidEye	Band 2
08/09/2020	Pléiades	PAN, resampled from 0.5 m

Table A2. Processed declassified scenes from reconnaissance satellites.

Date (dd/mm/yyyy)	Sensor	ID	Notes
18/08/1968	KH-4 PC	DS1104-2169DA097	
		DS1104-2169DF091	
17/08/1972	KH-9 PC	D3C1203-400520A048	
		D3C1203-400520F048	
		DS1104-2169DF091	
16/07/1973	KH-9 MC	DZB1206-500007L015001	
		DZB1206-500007L016001	
22/11/1973	KH-9 MC	DZB1207-500041L001001	Tristereo
		DZB1207-500041L002001	
		DZB1207-500041L003001	
11/06/1975	KH-9 PC	D3C1210-100030A111	
		D3C1210-100030F111	
25/07/1980	KH-9 PC	D3C1216-200279A037	
		D3C1216-200279F036	
20/08/1980	KH-9 MC	DZB1216-500273L006001	Tristereo
		DZB1216-500273L007001	
		DZB1216-500273L008001	

Appendix B: Orthorectification of SPOT scenes

Our workflow for SPOT orthorectification is closely based on the geoCosiCorr3D pipeline of Aati et al. (2022). The main difference is the use of NASA ASP tools (instead of Mic-Mac) for tie point detection between the raw and reference images. We adopted this change because of the observed inability of MicMac to obtain a sufficient number of tie points between Pléiades and SPOT scenes. Thus, we initially derived tie points by using NASA ASP tools *ipfind* and *ipmatch* between the raw SPOT images and the Pléiades 2020 reference, downsampled to match the SPOT resolution (Table 2). However, monoscopic SPOT scenes have a 60×60 km footprint which extends significantly beyond the Pléiades coverage, as well as highly variable cloud and snow cover. These traits complicated the automatic detection of sufficient well-distributed GCPs from the Pléiades scene, limiting the accuracy of the result or even preventing successful orthorectification in some cases. Thus, with the Pléiades reference, we orthorectified just two cloud-free scenes from SPOT 5 HRG, collected in 2006: a winter one with favorable illumination conditions and a late-summer one with similar snow cover to that from Pléiades. We then adopted the resulting orthoimages as reference for all other (winter and summer) SPOT scenes. The ample overlap enabled GCP detection even with challenging snow and cloud cover conditions. After matching the tie points, we discarded those falling close to unstable terrain or to the scene margins (since patch correlation is used in geoCosiCorr3D for RSM refinement). In most cases, this selection still left several hundred unevenly distributed tie points. To optimize both spatial coverage and processing performance, we limited the number of matches to 60 for each scene. After random selection of the first point, we iteratively selected the next one based on maximization of the average horizontal distance to the already-selected points. This ensured complete and uniform spatial coverage of each scene (Fig. B1). We converted tie points to GCPs by extracting their elevation from NASADEM. Finally, we processed all sets of scenes and GCPs with the RSM refinement and orthorectification of geoCosiCorr3D (Aati et al., 2022).

We observed a rather strong dependence of the GCP spatial distribution (and thus orthorectification result) on the parameters of ipfind and ipmatch: N is the target number of feature points to be detected, and T_m is the threshold for random sample consensus (RANSAC) of point matching. Specifically, the value of N must be sufficiently large to enable detection of enough tie points, even on scenes with large snow cover or small overlap with the reference. At the same time, a very large N and small T_m tended to produce GCPs clustered within narrow subregions of the images, with a low matching error but incomplete spatial coverage, and subsequently inaccurate orthorectification. Finally, a large value of T_m sometimes failed to exclude wrongly matched tie points, also leading to imprecise orthorectification. Thus, we ran the pipeline with multiple values of N and T_m (within $[10^5, 10^7]$

and $[10, 100]$, respectively); for each scene, we selected the parameter combination with the lowest residual error among those with full GCP coverage of the overlap region between raw and reference scene.

For orthorectification of all monoscopic scenes, including SPOT, we used the NASADEM topography as reference terrain. Such a single DEM does not reflect surface height change over the years, potentially leading to horizontal biases in the resulting glacier imagery (Kääb et al., 2016). In Sect. 2.2.2, we generate SPOT 5 HRS DEMs, which in several cases match the date of monoscopic HRG scenes, providing a simultaneous terrain surface for orthorectification. However, such DEMs have inconsistent coverage and present gaps and errors from pixel saturation and stereo-matching blunders. Thus, using them for orthorectification would involve nontrivial mosaicking and interpolation, again leading to orthoimage distortion. Moreover, the Abramov glacier tongue (where height change is largest) follows an overall NNE orientation of $14°$, which matches within $\pm 1°$ the local ground track of sun-synchronous satellites (Capderou, 2005). In other words, ice flow is parallel to the satellite track, while horizontal biases introduced by an inaccurate DEM mainly affect the cross-track direction for nadir acquisitions (Kääb et al., 2016). As such, we expect only minimal impact on our derived surface velocities. We verified this conclusion by testing orthorectification with the Copernicus GLO-30 terrain instead of NASADEM (average 13 ± 5 m height difference over the glacier tongue). Over 2005–2006 (Fig. 4a), the bias of derived velocity is between -0.2 and $+1.0\%$, well within uncertainty range.
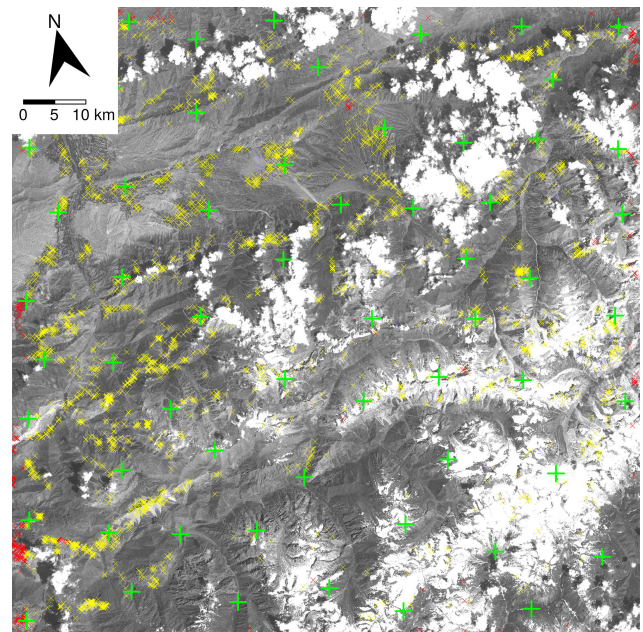

Figure B1. Raw SPOT 5 HRG scene from 3 August 2005. Green marks are the final selection of GCPs for orthorectification; red and yellow indicate, respectively, discarded and excess tie points.

Appendix C: SPOT DEM generation

We calculated SPOT DEMs with NASA ASP using the GLO-90 DEM as the initial terrain guess. We also tested GLO-30 but found the occurrence of ghosting artifacts in the output when generated from such a higher-resolution seed (Beyer et al., 2025, p. 32). The 8 bit HRS scenes commonly suffer from pixel saturation over snow-covered areas (Barrou Dumont et al., 2024), in principle leading to data gaps on glacier accumulation areas in summer. However, we observed a tendency of the MGM algorithm to compute height values even in fully saturated areas, due to interpolation of voids in the disparity maps (Dehecq et al., 2020). Thus, we postprocessed each HRS DEM by discarding all pixels corresponding to saturated digital numbers in the respective input scenes. We subsequently coregistered the full DEMs to NASADEM with the approach in Nuth and Kääb (2011) followed by a 2D tilt correction (Girod et al., 2017), using RGI outlines as unstable terrain. In four cases we found Abramov glacier to be split over two overlapping stereo pairs, acquired at a few minutes of interval. In the corresponding DEMs, we observed seam artifacts at the edges, preventing a straightforward mosaicking. We corrected the artifacts by introducing a second step of fine local coregistration of these split DEMs to NASADEM, applied only within a reduced region around Abramov. Because of increased terrain ruggedness and instability in this mountainous region compared with the full HRS scenes, we used a more restrictive definition of stable terrain: we excluded a 200 m buffer around the RGI outlines, all slopes greater than 30° (Denzinger et al., 2021), and all cells with an elevation difference greater than four NMADs before coregistration. Then we mosaicked the coregistered DEM pairs, using simple arithmetic average over the regions of overlap. In all cases the seam artifact at Abramov disappeared. In order to obtain a DEM with full glacier coverage, we also combined two short-interval HRS DEMs, from 1 and 6 August 2003. The former was acquired at a low gain setting, preserving details over the snow-covered accumulation area, while the latter provides cloud-free coverage of the lower tongue: the combination achieved a DEM with elevation data on more than 99.9 % of the glacier extent that we used in ice thickness and volume comparisons (Figs. 5 and 6a). This DEM, together with all 5 d interval HRS DEMs, also allowed us to evaluate the stability of HRS DEM results both on-glacier and off-glacier (Sects. 2.2.2 and 3.3.1, Fig. C1).

Appendix D: Flow continuity

We checked the consistency of our estimated ice velocities and volume changes by means of the continuity equation applied to the terminus region of the glacier (Fig. 5b). Assuming no change in bed separation, ice influx to the terminus can be expressed in discrete form, integrated over both time
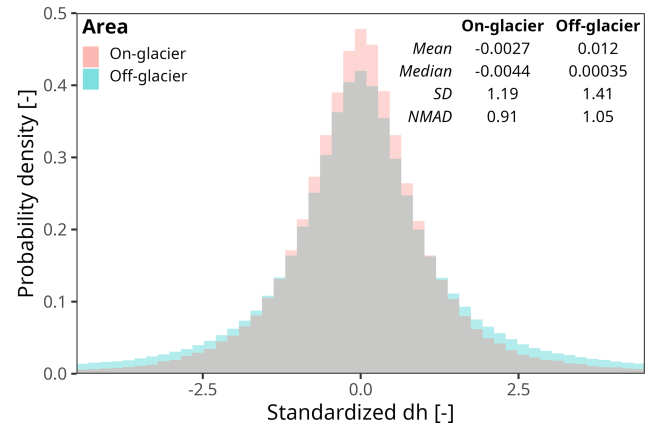
Figure C1. On-glacier and off-glacier distribution of standardized elevation differences within HRS DEM pairs at 5 d intervals.

and space (Reynaud et al., 1986; van der Veen, 2013):

$$Q = \left(\overline{\Delta H} - \frac{\overline{B}}{\rho_i}\right) \cdot A = k\Delta t \sum_{i=1}^{N} u_{s,i} H_i L_i, \tag{D1}$$

where $\overline{\Delta H}$ is the surface height change and $\overline{B}$ the surface mass balance, both averaged over the terminus region of area A and measured over period Δt; ρ_i is ice density; summation is performed over the $i = 1, \ldots, N$ segments of a transverse flux gate at the upper boundary of the terminus region; $u_{s,i}$ is the ice surface velocity perpendicular to the flux gate; H_i is the corresponding ice thickness; L_i is the length of the transverse segment; and k is the mean ratio between depth-averaged and surface velocity. We derived $\overline{\Delta H}$ from DEM differentiation (Sect. 2.3.3), $\overline{B}$ from the daily model of Kronenberg et al. (2022), u_i from the ice velocities of Sect. 2.3.2, and H_i from the bed map of Kuz'michenok et al. (1992). Thus, in Eq. (D1), the ratio k remains the only unknown parameter. We computed this by inverting the equation over the subperiods for which all required variables were simultaneously available: the three annual intervals between 6 August 2003, 9 July 2004, 3 August 2005, and 2 August 2006. We computed uncertainties in our remote sensing data as per Sect. 2.3.2 and 2.3.3; in the surface mass balance, from the RMSE between the model of Kronenberg et al. (2022) and the glaciological measurements (0.7 m w.e. yr^{-1}); in the ice thicknesses, with a conservative $\pm$ 20 % based on literature values (e.g., Grab et al., 2021); and in the ratio k, with standard error propagation. From the left-hand side of Eq. (D1), we derived ice influx values of 5.4 ± 0.8, 2.3 ± 0.9, and $1.7 \pm 0.8 \times 10^6$ m^3, respectively, for 2003–2004, 2004–2005, and 2005–2006. The numbers refer to the terminus region downstream of the lower cross-section in Fig. 5b. To match those results using the right-hand side of Eq. (D1), we obtained the following ratios of depth-averaged to surface velocity: 0.95 ± 0.26, 0.67 ± 0.31, and 0.67 ± 0.38. Despite the large uncertainties, results are all within physical

ranges, confirming the consistency of our datasets. The high value for 2003–2004 corresponds to a dominant contribution of basal sliding, which brings depth-averaged velocity close to surface values (Cuffey and Paterson, 2010). Over the later years, the result is somewhat lower – but well within uncertainty range – when compared with the theoretical prediction of a simple shear profile: 0.8 in case of no basal sliding and 1.0 for slip-dominated motion (Cuffey and Paterson, 2010). Our value of 0.67 is also very close to the ratio (0.64) proposed by Suslov et al. (1980) at Abramov for the 1960s and 1970s before the first pulsation, reportedly based on Palgov (1958). Unfortunately, the data and reasoning behind such an estimate appear to never have been published – thus, we do not speculate further as to potential interpretations.

Appendix E: Abramov glacier dynamics within global remote sensing datasets
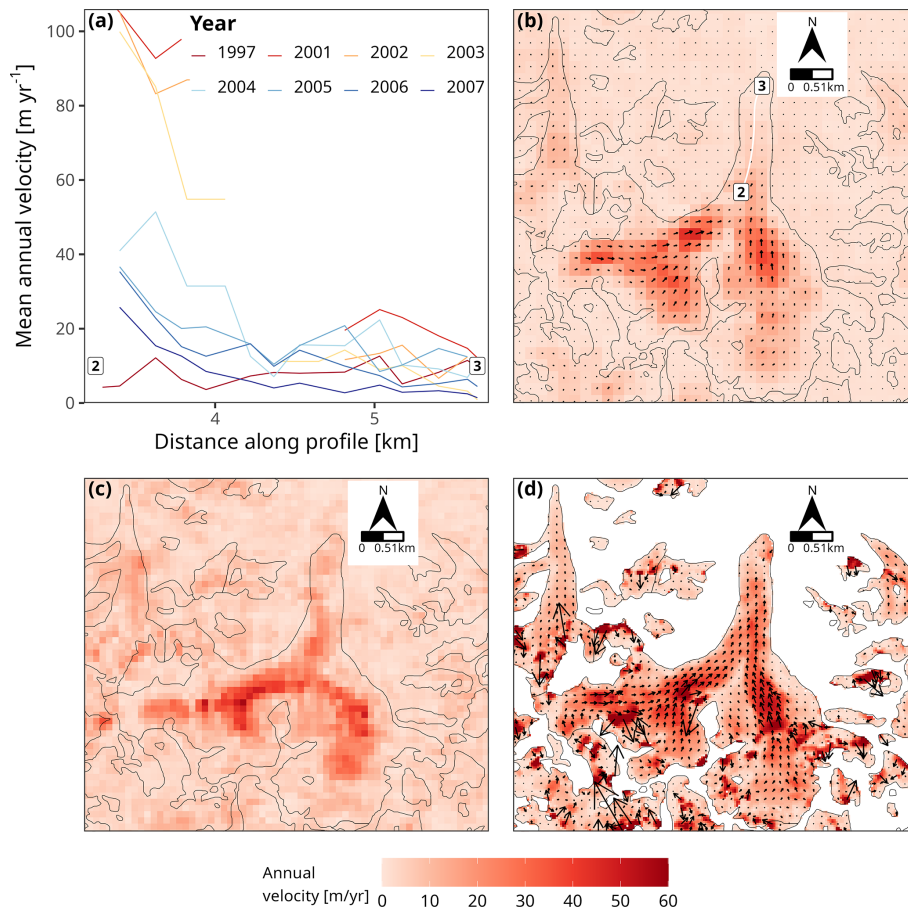
Figure E1. (a) Longitudinal profiles of mean annual surface velocity from ITS_LIVE (Gardner et al., 2024) during the second active phase. Profile geometry is shown in panel (b) and is the same as in Fig. 4b. (b–d) Maps of mean annual surface velocity in 2017/18 (compare with Fig. 4b) from (b) ITS_LIVE, (c) Friedl et al. (2021), and (d) Millan et al. (2022). For readability, the vector field of flow velocity is sampled (with arrows) at different intervals across the plots: the original spatial resolution of the products is 240, 200, and 50 m, respectively.
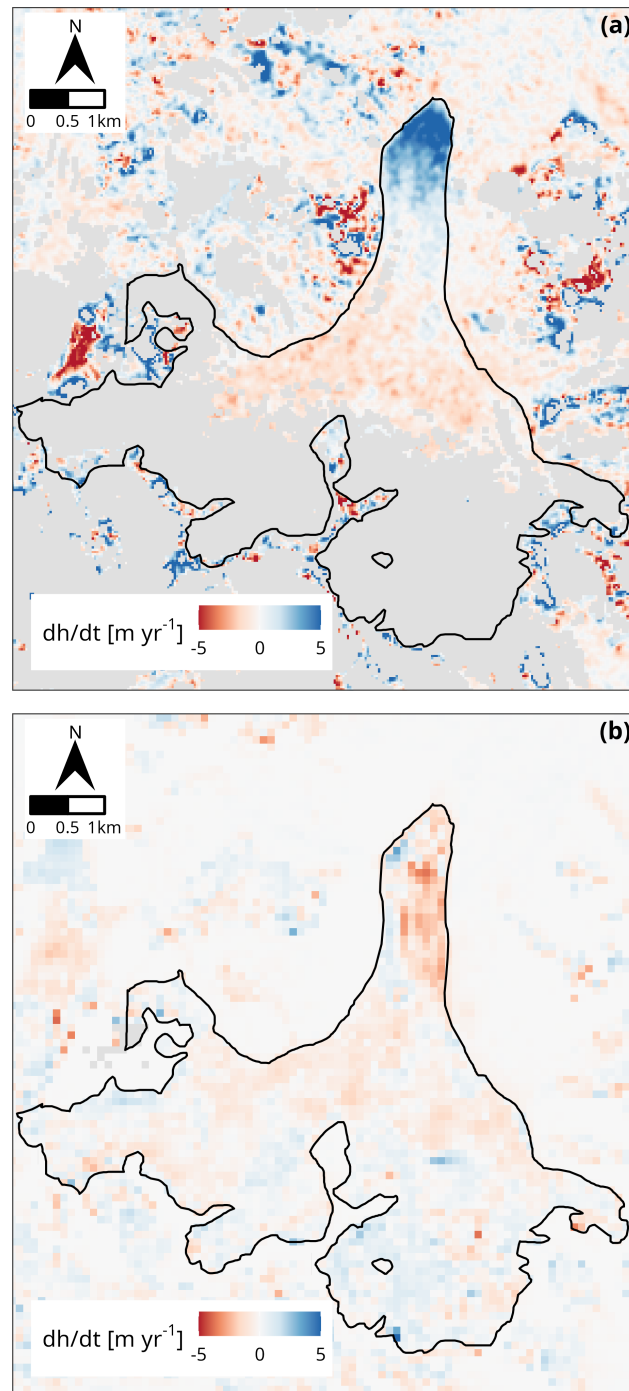
Figure E2. Annual surface height change rate over 2000–2005. **(a)** Our result, from NASADEM and SPOT. **(b)** Hugonnet et al. (2021), from ASTER.

Disclaimer. Publisher's note: Copernicus Publications remains neutral with regard to jurisdictional claims made in the text, published maps, institutional affiliations, or any other geographical representation in this paper. While Copernicus Publications makes every effort to include appropriate place names, the final responsibility lies with the authors.

References

Aati, S., Milliner, C., and Avouac, J.-P.: A new approach for 2-D and 3-D precise measurements of ground deformation from optimized registration and correlation of optical images and ICA-based filtering of image geometry artifacts, Remote Sens. Environ., 277, 113038, https://doi.org/10.1016/j.rse.2022.113038, 2022.

Abulkhasanova, A., Bassin, N., and Kamnyansky, G.: On some observed and possible changes in the tongue part of the Abramov glacier, Materialy gliatsiologicheskikh issledovaniy, 36, 206–210, 1979.

Altena, B. and Leinss, S.: Improved surface displacement estimation through stacking cross-correlation spectra from multi-channel imagery, Science of Remote Sensing, 6, 100070, https://doi.org/10.1016/j.srs.2022.100070, 2022.

Altena, B., Kääb, A., and Wouters, B.: Correlation dispersion as a measure to better estimate uncertainty in remotely sensed glacier displacements, The Cryosphere, 16, 2285–2300, https://doi.org/10.5194/tc-16-2285-2022, 2022.

Antrix Corporation Limited: Company Profile, https://www.antrix.co.in/company-profile (last access: 14 January 2025), 2019.

Azisov, E., Hoelzle, M., Vorogushyn, S., Saks, T., Usubaliev, R., Esenaman Uulu, M., and Barandun, M.: Reconstructed Centennial Mass Balance Change for Golubin Glacier, Northern Tien Shan, Atmosphere, 13, 954, https://doi.org/10.3390/atmos13060954, 2022.

Bannwart, J., Piermattei, L., Dussaillant, I., Krieger, L., Floricioiu, D., Berthier, E., Roeoesli, C., Machguth, H., and Zemp, M.: Elevation bias due to penetration of spaceborne radar signal on Grosser Aletschgletscher, Switzerland, J. Glaciol., 70, e1, https://doi.org/10.1017/jog.2024.37, 2024.

Barandun, M. and Pohl, E.: Central Asia's spatiotemporal glacier response ambiguity due to data inconsistencies and regional simplifications, The Cryosphere, 17, 1343–1371, https://doi.org/10.5194/tc-17-1343-2023, 2023.

Barandun, M., Huss, M., Sold, L., Farinotti, D., Azisov, E., Salzmann, N., Usubaliev, R., Merkushkin, A., and Hoelzle, M.: Re-analysis of seasonal mass balance at Abramov glacier 1968–2014, J. Glaciol., 61, 1103–1117, https://doi.org/10.3189/2015JoG14J239, 2015.

Barandun, M., Huss, M., Usubaliev, R., Azisov, E., Berthier, E., Kääb, A., Bolch, T., and Hoelzle, M.: Multi-decadal mass balance series of three Kyrgyz glaciers inferred from modelling constrained with repeated snow line observations, The Cryosphere, 12, 1899–1919, https://doi.org/10.5194/tc-12-1899-2018, 2018.

Barandun, M., Fiddes, J., Scherler, M., Mathys, T., Saks, T., Petrakov, D., and Hoelzle, M.: The state and future of the cryosphere in Central Asia, Water Security, 11, 100072, https://doi.org/10.1016/j.wasec.2020.100072, 2020.

Barandun, M., Pohl, E., Naegeli, K., McNabb, R., Huss, M., Berthier, E., Saks, T., and Hoelzle, M.: Hot Spots of Glacier Mass Balance Variability in Central Asia, Geophys. Res. Lett., 48, e2020GL092084, https://doi.org/10.1029/2020GL092084, 2021.

Barrou Dumont, Z., Gascoin, S., and Inglada, J.: Snow and Cloud Classification in Historical SPOT Images: An Image Emulation Approach for Training a Deep Learning Model Without Reference Data, IEEE J. Sel. Top. Appl., 17, 5541–5552, https://doi.org/10.1109/JSTARS.2024.3361838, 2024.

Bassin, N. and Kamnyansky, G.: Reconstruction of morphometric characteristics of Abramov Glacier, Transactions of the Central Asian Regional Research Institute (SARNII), 123, 84–93, 1987.

Beaud, F., Aati, S., Delaney, I., Adhikari, S., and Avouac, J.-P.: Surge dynamics of Shisper Glacier revealed by time-series correlation of optical satellite images and their utility to substantiate a generalized sliding law, The Cryosphere, 16, 3123–3148, https://doi.org/10.5194/tc-16-3123-2022, 2022.

Benn, D. I., Fowler, A. C., Hewitt, I., and Sevestre, H.: A general theory of glacier surges, J. Glaciol., 65, 701–716, https://doi.org/10.1017/jog.2019.62, 2019.

Berthier, E., Arnaud, Y., Baratoux, D., Vincent, C., and Rémy, F.: Recent rapid thinning of the "Mer de Glace" glacier derived from satellite optical images, Geophys. Res. Lett., 31, 2004GL020706, https://doi.org/10.1029/2004GL020706, 2004.

Berthier, E., Vincent, C., Magnússon, E., Gunnlaugsson, Á. Þ., Pitte, P., Le Meur, E., Masiokas, M., Ruiz, L., Pálsson, F., Belart, J. M. C., and Wagnon, P.: Glacier topography and elevation changes derived from Pléiades sub-meter stereo images, The Cryosphere, 8, 2275–2291, https://doi.org/10.5194/tc-8-2275-2014, 2014.

Berthier, E., Cabot, V., Vincent, C., and Six, D.: Decadal Region-Wide and Glacier-Wide Mass Balances Derived from Multi-Temporal ASTER Satellite Digital Elevation Models. Validation over the Mont-Blanc Area, Frontiers in Earth Science, 4, 63, https://doi.org/10.3389/feart.2016.00063, 2016.

Berthier, E., Vincent, C., and Six, D.: Exceptional thinning through the entire altitudinal range of Mont-Blanc glaciers during the 2021/22 mass balance year, J. Glaciol., 70, e30, https://doi.org/10.1017/jog.2023.100, 2023.

Berthier, E., Lebreton, J., Fontannaz, D., Hosford, S., Belart, J. M.-C., Brun, F., Andreassen, L. M., Menounos, B., and Blondel, C.: The Pléiades Glacier Observatory: high-resolution digital elevation models and ortho-imagery to monitor glacier change, The Cryosphere, 18, 5551–5571, https://doi.org/10.5194/tc-18-5551-2024, 2024.

Beyer, R. A., Alexandrov, O., and McMichael, S.: The Ames Stereo Pipeline: NASA's Open Source Software for Deriving and Processing Terrain Data, Earth and Space Science, 5, 537–548, https://doi.org/10.1029/2018EA000409, 2018.

Beyer, R. A., Alexandrov, O., McMichael, S., and the ASP contributors: Ames Stereo Pipeline Documentation, United States Government as represented by the Administrator of the National Aeronautics and Space Administration, https://stereopipeline.readthedocs.io/en/stable/examples/spot5.html, last access: 14 January 2025.

Bhambri, R., Hewitt, K., Kawishwar, P., and Pratap, B.: Surge-type and surge-modified glaciers in the Karakoram, Scientific Reports, 7, 15391, https://doi.org/10.1038/s41598-017-15473-8, 2017.

Bhattacharya, A., Bolch, T., Mukherjee, K., King, O., Menounos, B., Kapitsa, V., Neckel, N., Yang, W., and Yao, T.: High Mountain Asian glacier response to climate revealed by multi-temporal satellite observations since the 1960s, Nat. Commun., 12, 4133, https://doi.org/10.1038/s41467-021-24180-y, 2021.

Bhushan, S. and Shean, D.: Chamoli Disaster Pre-event 2-m DEM Composite: September 2015, Zenodo [data set], https://doi.org/10.5281/zenodo.4554647, 2021.

Bolch, T., Pieczonka, T., and Benn, D. I.: Multi-decadal mass loss of glaciers in the Everest area (Nepal Himalaya) derived from stereo imagery, The Cryosphere, 5, 349–358, https://doi.org/10.5194/tc-5-349-2011, 2011.

Bolch, T., Pieczonka, T., Mukherjee, K., and Shea, J.: Brief communication: Glaciers in the Hunza catchment (Karakoram) have been nearly in balance since the 1970s, The Cryosphere, 11, 531–539, https://doi.org/10.5194/tc-11-531-2017, 2017.

Brun, F., Berthier, E., Wagnon, P., Kääb, A., and Treichler, D.: A spatially resolved estimate of High Mountain Asia glacier mass balances from 2000 to 2016, Nat. Geosci., 10, 668–673, https://doi.org/10.1038/ngeo2999, 2017.

Buckley, S., Agram, P., Belz, J., Crippen, R., Gurrola, E., Hensley, S., Kobrick, M., Lavalle, M., Martin, J., Neumann, M., Nguyen, Q., Rosen, P., Shimada, J., Simard, M., and Tung, W.: NASADEM: user guide, Tech. Rep., NASA JPL, Pasadena, California, https://lpdaac.usgs.gov/documents/1318/NASADEM_User_Guide_V12.pdf (last access: 14 January 2025), 2023.

Capderou, M.: Satellites – orbits and missions, Springer, Berlin Heidelberg, ISBN 978-2-287-21317-5, 2005.

Chudley, T. R. and Willis, I. C.: Glacier surges in the north-west West Kunlun Shan inferred from 1972 to 2017 Landsat imagery, J. Glaciol., 65, 1–12, https://doi.org/10.1017/jog.2018.94, 2019.

Cogley, J.: Geodetic and direct mass-balance measurements: comparison and joint analysis, Ann. Glaciol., 50, 96–100, https://doi.org/10.3189/172756409787769744, 2009.

Copland, L., Sylvestre, T., Bishop, M. P., Shroder, J. F., Seong, Y. B., Owen, L. A., Bush, A., and Kamp, U.: Expanded and Recently Increased Glacier Surging in the Karakoram, Arct. Antarct. Alp. Res., 43, 503–516, https://doi.org/10.1657/1938-4246-43.4.503, 2011.

Cox, L. H. and March, R. S.: Comparison of geodetic and glaciological mass-balance techniques, Gulkana Glacier, Alaska, U.S.A., J. Glaciol., 50, 363–370, https://doi.org/10.3189/172756504781829855, 2004.

Cuffey, K. and Paterson, W. S. B.: The physics of glaciers, Butterworth-Heinemann/Elsevier, Burlington, MA, 4th edn., ISBN 978-0-12-369461-4, oCLC: ocn488732494, 2010.

Dehecq, A., Millan, R., Berthier, E., Gourmelen, N., Trouve, E., and Vionnet, V.: Elevation Changes Inferred From TanDEM-X Data Over the Mont-Blanc Area: Impact of the X-Band Interferometric Bias, IEEE J. Sel. Top. Appl., 9, 3870–3882, https://doi.org/10.1109/JSTARS.2016.2581482, 2016.

Dehecq, A., Gardner, A. S., Alexandrov, O., McMichael, S., Hugonnet, R., Shean, D., and Marty, M.: Automated Processing of Declassified KH-9 Hexagon Satellite Images for Global Elevation Change Analysis Since the 1970s, Frontiers in Earth Science, 8, 566802, https://doi.org/10.3389/feart.2020.566802, 2020.

Denzinger, F., Machguth, H., Barandun, M., Berthier, E., Girod, L., Kronenberg, M., Usubaliev, R., and Hoelzle, M.: Geodetic mass balance of Abramov Glacier from 1975 to 2015, J. Glaciol., 67, 331–342, https://doi.org/10.1017/jog.2020.108, 2021.

Deschamps-Berger, C., Gascoin, S., Berthier, E., Deems, J., Gutmann, E., Dehecq, A., Shean, D., and Dumont, M.: Snow depth mapping from stereo satellite imagery in mountainous terrain: evaluation using airborne laser-scanning data, The Cryosphere, 14, 2925–2940, https://doi.org/10.5194/tc-14-2925-2020, 2020.

Dolgoushin, L. and Osipova, G.: Pulsating glaciers, Hydrometeoizdat, Leningrad, 192 pp., https://www.libex.ru/detail/book1149760.html (last access: 16 January 2025), 1982.

Dolgoushin, L. D. and Osipova, G. B.: Glacier surges and the problem of their forecasting, in: Proceedings of the Moscow Symposium, August 1971, vol. 104, IAHS-AISH, Moscow, 1975.

Dowdeswell, J. A., Hodgkins, R., Nuttall, A., Hagen, J. O., and Hamilton, G. S.: Mass balance change as a control on the frequency and occurrence of glacier surges in Svalbard, Norwegian High Arctic, Geophys. Res. Lett., 22, 2909–2912, https://doi.org/10.1029/95GL02821, 1995.

Drusch, M., Del Bello, U., Carlier, S., Colin, O., Fernandez, V., Gascon, F., Hoersch, B., Isola, C., Laberinti, P., Martimort, P., Meygret, A., Spoto, F., Sy, O., Marchese, F., and Bargellini, P.: Sentinel-2: ESA's Optical High-Resolution Mission for GMES Operational Services, Remote Sens. Environ., 120, 25–36, https://doi.org/10.1016/j.rse.2011.11.026, 2012.

Dussaillant, I., Berthier, E., and Brun, F.: Geodetic Mass Balance of the Northern Patagonian Icefield from 2000 to 2012 Using Two Independent Methods, Frontiers in Earth Science, 6, 8, https://doi.org/10.3389/feart.2018.00008, 2018.

Earth Resources Observation And Science (EROS) Center: Declassified Satellite Imagery – 1, USGS [data set], https://doi.org/10.5066/F78P5XZM, 2017a.

Earth Resources Observation And Science (EROS) Center: Declassified Satellite Imagery – 2, USGS [data set], https://doi.org/10.5066/F74X5684, 2017b.

Earth Resources Observation And Science (EROS) Center: Declassified Satellite Imagery – 3, USGS [data set], https://doi.org/10.5066/F7WD3Z10, 2017c.

Eisen, O., Harrison, W. D., and Raymond, C. F.: The surges of Variegated Glacier, Alaska, U.S.A., and their connection to climate and mass balance, J. Glaciol., 47, 351–358, https://doi.org/10.3189/172756501781832179, 2001.

Emelyianov, Y., Nozdriukhin, V., and Suslov, V.: Dynamics of the Abramov Glacier during the 1972–1973 surge, Materialy gliatsiologicheskikh issledovaniy, 24, 87–96, 1974.

European Space Agency: S2 Processing Baseline – Sentinel Online, https://sentinels.copernicus.eu/web/sentinel/technical-guides/sentinel-2-msi/processing-baseline (last access: 14 January 2025), 2024.

European Space Agency and Airbus: Copernicus DEM, European Space Agency, European Space Agency [data set], https://doi.org/10.5270/ESA-c5d3d65, 2022.

Facciolo, G., Franchis, C., and Meinhardt, E.: MGM: a significantly more global matching for stereo vision, in: Proc. British Machine Vision Conf., Swansea, UK, 7–10 September 2015, http://dev.ipol.im/~facciolo/mgm/mgm.pdf (last access: 14 January 2025), 2015.

Fahrland, E.: Copernicus Digital Elevation Model Product Handbook (v4.0), Tech. Rep. AO/1-9422/18/I-LG, Airbus Defence and Space GmbH, Taufkirchen, Germany, https://dataspace.copernicus.eu/sites/default/files/media/files/2024-06/geo1988-copernicusdem-spe-002_producthandbook_i5.0.pdf (last access: 14 January 2025), 2022.

Falaschi, D., Berthier, E., Belart, J. M. C., Bravo, C., Castro, M., Durand, M., and Villalba, R.: Increased mass loss of glaciers in Volcán Domuyo (Argentinian Andes) between 1962 and 2020, revealed by aerial photos and satellite stereo imagery, J. Glaciol., 69, 40–56, https://doi.org/10.1017/jog.2022.43, 2023.

Fan, Y., Ke, C.-Q., Zhou, X., Shen, X., Yu, X., and Lhakpa, D.: Glacier mass-balance estimates over High Mountain Asia from 2000 to 2021 based on ICESat-2 and NASADEM, J. Glaciol., 69, 500–512, https://doi.org/10.1017/jog.2022.78, 2023.

Farinotti, D., Longuevergne, L., Moholdt, G., Duethmann, D., Mölg, T., Bolch, T., Vorogushyn, S., and Güntner, A.: Substantial glacier mass loss in the Tien Shan over the past 50 years, Nat. Geosci., 8, 716–722, https://doi.org/10.1038/ngeo2513, 2015.

Fisher, A.: Cloud and Cloud-Shadow Detection in SPOT5 HRG Imagery with Automated Morphological Feature Extraction, Remote Sensing, 6, 776–800, https://doi.org/10.3390/rs6010776, 2014.

Fitch, A., Kadyrov, A., Christmas, W., and Kittler, J.: Orientation Correlation, in: Procedings of the British Machine Vision Conference 2002, 2–5 September 2002, British Machine Vision Association, Cardiff, ISBN 978-1-901725-19-3, https://web.archive.org/web/20231010071245/https://dblp.org/db/conf/bmvc/bmvc2002.html (last access: 16 January 2025), 2002.

Flowers, G. E., Roux, N., Pimentel, S., and Schoof, C. G.: Present dynamics and future prognosis of a slowly surging glacier, The Cryosphere, 5, 299–313, https://doi.org/10.5194/tc-5-299-2011, 2011.

Fowler, A. C., Murray, T., and Ng, F. S. L.: Thermally controlled glacier surging, J. Glaciol., 47, 527–538, https://doi.org/10.3189/172756501781831792, 2001.

Friedl, P., Seehaus, T., and Braun, M.: Global time series and temporal mosaics of glacier surface velocities derived from Sentinel-1 data, Earth Syst. Sci. Data, 13, 4653–4675, https://doi.org/10.5194/essd-13-4653-2021, 2021.

Gardelle, J., Berthier, E., and Arnaud, Y.: Impact of resolution and radar penetration on glacier elevation changes computed from DEM differencing, J. Glaciol., 58, 419–422, https://doi.org/10.3189/2012JoG11J175, 2012.

Gardelle, J., Berthier, E., Arnaud, Y., and Kääb, A.: Region-wide glacier mass balances over the Pamir-Karakoram-Himalaya during 1999–2011, The Cryosphere, 7, 1263–1286, https://doi.org/10.5194/tc-7-1263-2013, 2013.

Gardner, A., Fahnestock, M., and Scambos, T.: ITS_LIVE Regional Glacier and Ice Sheet Surface Velocities, Version 1, NSIDC [data set], https://doi.org/10.5067/6II6VW8LLWJ7, 2024.

Gardner, A. S., Moholdt, G., Cogley, J. G., Wouters, B., Arendt, A. A., Wahr, J., Berthier, E., Hock, R., Pfeffer, W. T., Kaser, G., Ligtenberg, S. R. M., Bolch, T., Sharp, M. J., Hagen, J. O., Van Den Broeke, M. R., and Paul, F.: A Reconciled Estimate of Glacier Contributions to Sea Level Rise: 2003 to 2009, Science, 340, 852–857, https://doi.org/10.1126/science.1234532, 2013.

Gardner, A. S., Moholdt, G., Scambos, T., Fahnstock, M., Ligtenberg, S., van den Broeke, M., and Nilsson, J.: Increased West Antarctic and unchanged East Antarctic ice discharge over the last 7 years, The Cryosphere, 12, 521–547, https://doi.org/10.5194/tc-12-521-2018, 2018.

Ghuffar, S., Bolch, T., Rupnik, E., and Bhattacharya, A.: A Pipeline for Automated Processing of Declassified Corona KH-4 (1962–1972) Stereo Imagery, IEEE T. Geosci. Remote, 60, 1–14, https://doi.org/10.1109/TGRS.2022.3200151, 2022.

Ghuffar, S., King, O., Guillet, G., Rupnik, E., and Bolch, T.: Brief communication: Glacier mapping and change estimation using very high-resolution declassified Hexagon KH-9 panoramic stereo imagery (1971–1984), The Cryosphere, 17, 1299–1306, https://doi.org/10.5194/tc-17-1299-2023, 2023.

Girod, L., Nuth, C., Kääb, A., Etzelmüller, B., and Kohler, J.: Terrain changes from images acquired on opportunistic flights by SfM photogrammetry, The Cryosphere, 11, 827–840, https://doi.org/10.5194/tc-11-827-2017, 2017.

Glazirin', G.: Identification of surging glaciers by morphometric characteristics, Materialy gliatsiologicheskikh issledovaniy, 33, 136–138, 1978.

Glazirin', G. and Shchetinnikov, A.: Pulsating glaciers of the Gissar-Alay Mountains, Trudy sredneaziatskiy regional'nyy nauchno-issledovatel'skiy institut, 71, 81–100, 1980.

Glazirin', G., Kamnyansky, G., Mazo, A., Nozdriukhin, V., and Salamatin, A.: Mechanism of the Abramov glacier advance in 1972–1975, Materialy gliatsiologicheskikh issledovaniy, 60, 84–90, 1987.

Glazirin', G., Kamnyansky, G., and Pertziger, F.: The regime of Abramov glacier, Hydrometeoizdat, St Petersburg, 228 pp., ISBN 5-286-00952-2, 1993 (in Russian).

Goerlich, F., Bolch, T., Mukherjee, K., and Pieczonka, T.: Glacier Mass Loss during the 1960s and 1970s in the Ak-Shirak Range (Kyrgyzstan) from Multiple Stereoscopic Corona and Hexagon Imagery, Remote Sensing, 9, 275, https://doi.org/10.3390/rs9030275, 2017.

Goerlich, F., Bolch, T., and Paul, F.: More dynamic than expected: an updated survey of surging glaciers in the Pamir, Earth Syst. Sci. Data, 12, 3161–3176, https://doi.org/10.5194/essd-12-3161-2020, 2020.

Grab, M., Mattea, E., Bauder, A., Huss, M., Rabenstein, L., Hodel, E., Linsbauer, A., Langhammer, L., Schmid, L.,

Church, G., Hellmann, S., Délèze, K., Schaer, P., Lathion, P., Farinotti, D., and Maurer, H.: Ice thickness distribution of all Swiss glaciers based on extended ground-penetrating radar data and glaciological modeling, J. Glaciol., 67, 1074–1092, https://doi.org/10.1017/jog.2021.55, 2021.

Grishin, V. and Abulkhasanova, A.: Results of determining the field of ice movement velocities and the thickness of the Abramov glacier, Trudy sredneaziatskiy regional'nyy nauchno-issledovatel'skiy institut, 107, 116–120, 1986.

Guillet, G., King, O., Lv, M., Ghuffar, S., Benn, D., Quincey, D., and Bolch, T.: A regionally resolved inventory of High Mountain Asia surge-type glaciers, derived from a multi-factor remote sensing approach, The Cryosphere, 16, 603–623, https://doi.org/10.5194/tc-16-603-2022, 2022.

Harrison, W. D. and Post, A. S.: How much do we really know about glacier surging?, Ann. Glaciol., 36, 1–6, https://doi.org/10.3189/172756403781816185, 2003.

Heid, T. and Kääb, A.: Evaluation of existing image matching methods for deriving glacier surface displacements globally from optical satellite imagery, Remote Sens. Environ., 118, 339–355, https://doi.org/10.1016/j.rse.2011.11.024, 2012.

Herreid, S. and Truffer, M.: Automated detection of unstable glacier flow and a spectrum of speedup behavior in the Alaska Range, J. Geophys. Res.-Earth, 121, 64–81, https://doi.org/10.1002/2015JF003502, 2016.

Hewitt, K.: Tributary glacier surges: an exceptional concentration at Panmah Glacier, Karakoram Himalaya, J. Glaciol., 53, 181–188, https://doi.org/10.3189/172756507782202829, 2007.

Hoelzle, M., Azisov, E., Barandun, M., Huss, M., Farinotti, D., Gafurov, A., Hagg, W., Kenzhebaev, R., Kronenberg, M., Machguth, H., Merkushkin, A., Moldobekov, B., Petrov, M., Saks, T., Salzmann, N., Schöne, T., Tarasov, Y., Usubaliev, R., Vorogushyn, S., Yakovlev, A., and Zemp, M.: Re-establishing glacier monitoring in Kyrgyzstan and Uzbekistan, Central Asia, Geosci. Instrum. Method. Data Syst., 6, 397–418, https://doi.org/10.5194/gi-6-397-2017, 2017.

Hoelzle, M., Barandun, M., Bolch, T., Fiddes, J., Gafurov, A., Muccione, V., Saks, T., and Shahgedanova, M.: The status and role of the alpine cryosphere in Central Asia, in: The Aral Sea Basin. Water for Sustainable Development in Central Asia, 100–121, Routledge, London, https://doi.org/10.4324/9780429436475-8, 2019.

Hoinkes, H. C.: Surges of the Vernagtferner in the Ötztal Alps since 1599, Can. J. Earth Sci., 6, 853–861, https://doi.org/10.1139/e69-086, 1969.

Hugonnet, R., McNabb, R., Berthier, E., Menounos, B., Nuth, C., Girod, L., Farinotti, D., Huss, M., Dussaillant, I., Brun, F., and Kääb, A.: Accelerated global glacier mass loss in the early twenty-first century, Nature, 592, 726–731, https://doi.org/10.1038/s41586-021-03436-z, 2021.

Hugonnet, R., Brun, F., Berthier, E., Dehecq, A., Mannerfelt, E. S., Eckert, N., and Farinotti, D.: Uncertainty Analysis of Digital Elevation Models by Spatial Inference From Stable Terrain, IEEE J. Sel. Top. Appl., 15, 6456–6472, https://doi.org/10.1109/JSTARS.2022.3188922, 2022.

Humphrey, N. F. and Raymond, C. F.: Hydrology, erosion and sediment production in a surging glacier: Variegated Glacier, Alaska, 1982–83, J. Glaciol., 40, 539–552, https://doi.org/10.3189/S0022143000012429, 1994.

Huss, M.: Density assumptions for converting geodetic glacier volume change to mass change, The Cryosphere, 7, 877–887, https://doi.org/10.5194/tc-7-877-2013, 2013.

Huss, M. and Hock, R.: Global-scale hydrological response to future glacier mass loss, Nat. Clim. Change, 8, 135–140, https://doi.org/10.1038/s41558-017-0049-x, 2018.

Jiskoot, H.: Glacier Surging, in: Encyclopedia of Snow, Ice and Glaciers, in: Encyclopedia of Earth Sciences Series, edited by: Singh, V. P., Singh, P., and Haritashya, U. K., Springer Netherlands, Dordrecht, 415–428, ISBN 978-90-481-2641-5, 978-90-481-2642-2, https://doi.org/10.1007/978-90-481-2642-2_559, 2011.

Kääb, A., Treichler, D., Nuth, C., and Berthier, E.: Brief Communication: Contending estimates of 2003–2008 glacier mass balance over the Pamir–Karakoram–Himalaya, The Cryosphere, 9, 557–564, https://doi.org/10.5194/tc-9-557-2015, 2015.

Kääb, A., Winsvold, S., Altena, B., Nuth, C., Nagler, T., and Wuite, J.: Glacier Remote Sensing Using Sentinel-2. Part I: Radiometric and Geometric Performance, and Application to Ice Velocity, Remote Sensing, 8, 598, https://doi.org/10.3390/rs8070598, 2016.

Kamb, B.: Glacier surge mechanism based on linked cavity configuration of the basal water conduit system, J. Geophys. Res.-Sol. Ea., 92, 9083–9100, https://doi.org/10.1029/JB092iB09p09083, 1987.

Kamnyansky, G.: Abramov glacier mass balance observations resume (1967–1998), Proceedings of SANIGMI, 161, 122–131, 2001.

Kasturirangan, K., Aravamudan, R., Deekshatulu, B., Joseph, G., and Chandrasekhar, M.: Indian remote sensing satellite (IRS)-1C – The beginning of a new era, Current Science, 70, 495–500, 1996.

Kenzhebaev, R., Barandun, M., Kronenberg, M., Chen, Y., Usubaliev, R., and Hoelzle, M.: Mass balance observations and reconstruction for Batysh Sook Glacier, Tien Shan, from 2004 to 2016, Cold Reg. Sci. Technol., 135, 76–89, https://doi.org/10.1016/j.coldregions.2016.12.007, 2017.

King, O., Ghuffar, S., Bhattacharya, A., Yao, R., Yao, T., and Bolch, T.: Glaciological and climatological drivers of heterogeneous glacier mass loss in the Tanggula Shan (Central-Eastern Tibetan Plateau), since the 1960s, J. Glaciol., 69, 1149–1166, https://doi.org/10.1017/jog.2023.5, 2023.

Kislov, B., Nozdriukhin, V., and Pertziger, F.: Temperature regime of the active layer of Abramov glacier, Materialy gliatsiologicheskikh issledovaniy, 30, 199–204, 1977.

Komatsu, T. and Watanabe, T.: Glacier-Related Hazards and Their Assessment in the Tajik Pamir: A Short Review, Geographical Studies, 88, 117–131, https://doi.org/10.7886/hgs.88.117, 2014.

Kotlyakov, V. M.: World atlas of snow and ice resources, Institute of Geography, Russian Academy of Sciences, Moscow, ISBN 9785891760103, 1997.

Kotlyakov, V. M., Chernova, L. P., Khromova, T. Y., and Zverkova, N. M.: Glacier surges and glacial disasters, Dokl. Earth Sci., 472, 57–61, https://doi.org/10.1134/S1028334X17010056, 2017.

Kronenberg, M., Barandun, M., Hoelzle, M., Huss, M., Farinotti, D., Azisov, E., Usubaliev, R., Gafurov, A., Petrakov, D., and Kääb, A.: Mass-balance reconstruction for Glacier No. 354, Tien Shan, from 2003 to 2014, Ann. Glaciol., 57, 92–102, https://doi.org/10.3189/2016AoG71A032, 2016.

Kronenberg, M., Machguth, H., Eichler, A., Schwikowski, M., and Hoelzle, M.: Comparison of historical and recent accumulation rates on Abramov Glacier, Pamir Alay, J. Glaciol., 67, 253–268, https://doi.org/10.1017/jog.2020.103, 2021.

Kronenberg, M., van Pelt, W., Machguth, H., Fiddes, J., Hoelzle, M., and Pertziger, F.: Long-term firn and mass balance modelling for Abramov Glacier in the data-scarce Pamir Alay, The Cryosphere, 16, 5001–5022, https://doi.org/10.5194/tc-16-5001-2022, 2022.

Kuglin, C. and Hines, D.: The phase correlation image alignment method, in: Proc. Int. Conf. Cybernetics Society, San Francisco, California, 23–25 September 1975, 163–165, http://boutigny.free.fr/Astronomie/AstroSources/Kuglin-Hines.pdf (last access: 14 January 2025), 1975.

Kuz'michenok, V., Vasilenko, E., Macheret, Y., and Moskalevskiy, M.: Ice thickness and subglacial topography of the Abramov Glacier based on data from low frequency radio echo sounding, Materialy gliatsiologicheskikh issledovaniy, 75, 63–68, 1992.

Lacroix, P., Bièvre, G., Pathier, E., Kniess, U., and Jongmans, D.: Use of Sentinel-2 images for the detection of precursory motions before landslide failures, Remote Sens. Environ., 215, 507–516, https://doi.org/10.1016/j.rse.2018.03.042, 2018.

Lea, J. M., Mair, D. W., and Rea, B. R.: Evaluation of existing and new methods of tracking glacier terminus change, J. Glaciol., 60, 323–332, https://doi.org/10.3189/2014JoG13J061, 2014.

Leprince, S., Barbot, S., Ayoub, F., and Avouac, J.-P.: Automatic and Precise Orthorectification, Coregistration, and Subpixel Correlation of Satellite Images, Application to Ground Deformation Measurements, IEEE T. Geosci. Remote, 45, 1529–1558, https://doi.org/10.1109/TGRS.2006.888937, 2007.

Li, C., Jiang, L., Liu, L., and Wang, H.: Regional and Altitude-Dependent Estimate of the SRTM C/X-Band Radar Penetration Difference on High Mountain Asia Glaciers, IEEE J. Sel. Top. Appl., 14, 4244–4253, https://doi.org/10.1109/JSTARS.2021.3070362, 2021.

Li, H., Zhao, J., Yan, B., Yue, L., and Wang, L.: Global DEMs vary from one to another: an evaluation of newly released Copernicus, NASA and AW3D30 DEM on selected terrains of China using ICESat-2 altimetry data, Int. J. Digit. Earth, 15, 1149–1168, https://doi.org/10.1080/17538947.2022.2094002, 2022.

Lv, M., Guo, H., Yan, J., Wu, K., Liu, G., Lu, X., Ruan, Z., and Yan, S.: Distinguishing Glaciers between Surging and Advancing by Remote Sensing: A Case Study in the Eastern Karakoram, Remote Sensing, 12, 2297, https://doi.org/10.3390/rs12142297, 2020a.

Lv, M., Quincey, D. J., Guo, H., King, O., Liu, G., Yan, S., Lu, X., and Ruan, Z.: Examining geodetic glacier mass balance in the eastern Pamir transition zone, J. Glaciol., 66, 927–937, https://doi.org/10.1017/jog.2020.54, 2020b.

Mandychev, A. N., Usubaliev, R. A., and Azisov, E. A.: Changes of the Abramov Glacier (Alay Ridge) from 1850 to 2014, Ice and Snow, 57, 326–333, https://doi.org/10.15356/2076-6734-2017-3-326-333, 2017.

Mannerfelt, E. S., Hugonnet, R., Dehecq, A., and the xdem contributors: xdem documentation: estimation and modelling of spatial variograms, https://xdem.readthedocs.io/en/stable/advanced_examples/plot_variogram_estimation_modelling.html (last access: 14 January 2025), 2024.

Mattea, E.: MatteaE/abramov_optical_remote_sensing: Initial pre-release (v1.0), Zenodo [code], https://doi.org/10.5281/zenodo.12731407, 2024.

Mattea, E., Berthier, E., Dehecq, A., Bolch, T., Bhattacharya, A., Ghuffar, S., Barandun, M., and Hoelzle, M.: Datasets associated with paper "Five decades of Abramov glacier dynamics reconstructed with multi-sensor optical remote sensing", by Enrico Mattea et al., Zenodo [data set], https://doi.org/10.5281/zenodo.14193059, 2024.

Maurer, J. M., Schaefer, J. M., Rupper, S., and Corley, A.: Acceleration of ice loss across the Himalayas over the past 40 years, Science Advances, 5, eaav7266, https://doi.org/10.1126/sciadv.aav7266, 2019.

Mayo, L.: Identification of unstable glaciers intermediate between normal and surging glaciers, Materialy gliatsiologicheskikh issledovaniy, 33, 133–135, 1978.

McNabb, R., Nuth, C., Kääb, A., and Girod, L.: Sensitivity of glacier volume change estimation to DEM void interpolation, The Cryosphere, 13, 895–910, https://doi.org/10.5194/tc-13-895-2019, 2019.

Meier, M. F. and Post, A.: What are glacier surges?, Can. J. Earth Sci., 6, 807–817, https://doi.org/10.1139/e69-081, 1969.

Miles, E. S., Watson, C. S., Brun, F., Berthier, E., Esteves, M., Quincey, D. J., Miles, K. E., Hubbard, B., and Wagnon, P.: Glacial and geomorphic effects of a supraglacial lake drainage and outburst event, Everest region, Nepal Himalaya, The Cryosphere, 12, 3891–3905, https://doi.org/10.5194/tc-12-3891-2018, 2018.

Millan, R., Mouginot, J., Rabatel, A., Jeong, S., Cusicanqui, D., Derkacheva, A., and Chekki, M.: Mapping Surface Flow Velocity of Glaciers at Regional Scale Using a Multiple Sensors Approach, Remote Sensing, 11, 2498, https://doi.org/10.3390/rs11212498, 2019.

Millan, R., Mouginot, J., Rabatel, A., and Morlighem, M.: Ice velocity and thickness of the world's glaciers, Nat. Geosci., 15, 124–129, https://doi.org/10.1038/s41561-021-00885-z, 2022.

Mitášová, H. and Hofierka, J.: Interpolation by regularized spline with tension: II. Application to terrain modeling and surface geometry analysis, Math. Geol., 25, 657–669, https://doi.org/10.1007/BF00893172, 1993.

Moon, T. and Joughin, I.: Changes in ice front position on Greenland's outlet glaciers from 1992 to 2007, J. Geophys. Res.-Earth, 113, 2007JF000927, https://doi.org/10.1029/2007JF000927, 2008.

Muccione, V. and Fiddes, J.: State of the knowledge on water resources and natural hazards under climate change in Central Asia and South Caucasus, Tech. Rep., Swiss Agency for Development and Cooperation, Bern, https://www.zora.uzh.ch/id/eprint/181441 (last access: 14 January 2025), 2019.

Mukherjee, K., Bolch, T., Goerlich, F., Kutuzov, S., Osmonov, A., Pieczonka, T., and Shesterova, I.: Surge-Type Glaciers in the Tien Shan (Central Asia), Arct. Antarct. Alp. Res., 49, 147–171, https://doi.org/10.1657/AAAR0016-021, 2017.

Murodov, M., Li, L., Safarov, M., Lv, M., Murodov, A., Gulakhmadov, A., Khusrav, K., and Qiu, Y.: A Comprehensive Examination of the Medvezhiy Glacier's Surges in West Pamir (1968–2023), Remote Sensing, 16, 1730, https://doi.org/10.3390/rs16101730, 2024.

NASA JPL: NASADEM Merged DEM Global 1 arc second V001, NASA EOSDIS Land Processes Distributed Active Archive Center [data set], https://doi.org/10.5067/MEASURES/NASADEM/NASADEM_HGT.001, 2020.

NASA/METI/AIST/Japan Spacesystems and U.S./Japan ASTER Science Team: ASTER Level 1A Data Set – Reconstructed, unprocessed instrument data, NASA EOSDIS Land Processes Distributed Active Archive Center [data set], https://doi.org/10.5067/ASTER/AST_L1A.003, 2001.

Nosavan, J., Moreau, A., and Hosford, S.: SPOT World Heritage catalogue: 30 years of SPOT 1-to-5 observation, EGU General Assembly 2020, Online, 4–8 May 2020, EGU2020-8275, https://doi.org/10.5194/egusphere-egu2020-8275, 2020.

Nuth, C. and Kääb, A.: Co-registration and bias corrections of satellite elevation data sets for quantifying glacier thickness change, The Cryosphere, 5, 271–290, https://doi.org/10.5194/tc-5-271-2011, 2011.

Oerlemans, J. and van Pelt, W. J. J.: A model study of Abrahamsenbreen, a surging glacier in northern Spitsbergen, The Cryosphere, 9, 767–779, https://doi.org/10.5194/tc-9-767-2015, 2015.

Okolie, C. J., Mills, J. P., Adeleke, A. K., Smit, J. L., Peppa, M. V., Altunel, A. O., and Arungwa, I. D.: Assessment of the global Copernicus, NASADEM, ASTER and AW3D digital elevation models in Central and Southern Africa, Geo-spatial Information Science, 27, 1362–1390, https://doi.org/10.1080/10095020.2023.2296010, 2024.

Palgov, N. N.: Determination of the thickness of mountain glaciers by the method of balances, Proceedings of the All-Union Geographical Society, 90, 170–174, 1958.

Paul, F.: Revealing glacier flow and surge dynamics from animated satellite image sequences: examples from the Karakoram, The Cryosphere, 9, 2201–2214, https://doi.org/10.5194/tc-9-2201-2015, 2015.

Paul, F., Barrand, N., Baumann, S., Berthier, E., Bolch, T., Casey, K., Frey, H., Joshi, S., Konovalov, V., Le Bris, R., Mölg, N., Nosenko, G., Nuth, C., Pope, A., Racoviteanu, A., Rastner, P., Raup, B., Scharrer, K., Steffen, S., and Winsvold, S.: On the accuracy of glacier outlines derived from remote-sensing data, Ann. Glaciol., 54, 171–182, https://doi.org/10.3189/2013AoG63A296, 2013.

Paul, F., Bolch, T., Kääb, A., Nagler, T., Nuth, C., Scharrer, K., Shepherd, A., Strozzi, T., Ticconi, F., Bhambri, R., Berthier, E., Bevan, S., Gourmelen, N., Heid, T., Jeong, S., Kunz, M., Lauknes, T. R., Luckman, A., Merryman Boncori, J. P., Moholdt, G., Muir, A., Neelmeijer, J., Rankl, M., VanLooy, J., and Van Niel, T.: The glaciers climate change initiative: Methods for creating glacier area, elevation change and velocity products, Remote Sens. Environ., 162, 408–426, https://doi.org/10.1016/j.rse.2013.07.043, 2015.

Paul, F., Bolch, T., Briggs, K., Kääb, A., McMillan, M., McNabb, R., Nagler, T., Nuth, C., Rastner, P., Strozzi, T., and Wuite, J.: Error sources and guidelines for quality assessment of glacier area, elevation change, and velocity products derived from satellite data in the Glaciers_cci project, Remote Sens. Environ., 203, 256–275, https://doi.org/10.1016/j.rse.2017.08.038, 2017.

Paul, F., Rastner, P., Azzoni, R. S., Diolaiuti, G., Fugazza, D., Le Bris, R., Nemec, J., Rabatel, A., Ramusovic, M., Schwaizer, G., and Smiraglia, C.: Glacier shrinkage in the Alps continues unabated as revealed by a new glacier inven-

tory from Sentinel-2, Earth Syst. Sci. Data, 12, 1805–1821, https://doi.org/10.5194/essd-12-1805-2020, 2020.

Paul, F., Piermattei, L., Treichler, D., Gilbert, L., Girod, L., Kääb, A., Libert, L., Nagler, T., Strozzi, T., and Wuite, J.: Three different glacier surges at a spot: what satellites observe and what not, The Cryosphere, 16, 2505–2526, https://doi.org/10.5194/tc-16-2505-2022, 2022.

PCI Geomatics Enterprises: About Orthoengine, https://catalyst.earth/catalyst-system-files/help/concepts/orthoengine_c/Chapter_13.html (last access: 25 November 2023), 2024.

Pertziger, F.: Abramov Glacier Data Reference Book: Climate, Runoff, Mass Balance, Central Asian Hydrometeorological Institute, Tashkent, 1996.

Pieczonka, T. and Bolch, T.: Region-wide glacier mass budgets and area changes for the Central Tien Shan between ∼ 1975 and 1999 using Hexagon KH-9 imagery, Global Planet. Change, 128, 1–13, https://doi.org/10.1016/j.gloplacha.2014.11.014, 2015.

Pitte, P., Berthier, E., Masiokas, M. H., Cabot, V., Ruiz, L., Ferri Hidalgo, L., Gargantini, H., and Zalazar, L.: Geometric evolution of the Horcones Inferior Glacier (Mount Aconcagua, Central Andes) during the 2002–2006 surge, J. Geophys. Res.-Earth, 121, 111–127, https://doi.org/10.1002/2015JF003522, 2016.

Pizer, S. M., Amburn, E. P., Austin, J. D., Cromartie, R., Geselowitz, A., Greer, T., Ter Haar Romeny, B., Zimmerman, J. B., and Zuiderveld, K.: Adaptive histogram equalization and its variations, Computer Vision, Graphics, and Image Processing, 39, 355–368, https://doi.org/10.1016/S0734-189X(87)80186-X, 1987.

Planet Labs: Education and Research Program, https://www.planet.com/markets/education-and-research/ (last access: 14 January 2025), 2024.

Popovnin, V., Gubanov, A., Satylkanov, R., and Ermenbayev, B.: Mass balance of the Sary-Tor Glacier reproduced from meteorological data, Ice and Snow, 61, 58–74, https://doi.org/10.31857/S2076673421010071, 2021.

Quincey, D. J., Glasser, N. F., Cook, S. J., and Luckman, A.: Heterogeneity in Karakoram glacier surges, J. Geophys. Res.-Earth, 120, 1288–1300, https://doi.org/10.1002/2015JF003515, 2015.

Racoviteanu, A. E., Paul, F., Raup, B., Khalsa, S. J. S., and Armstrong, R.: Challenges and recommendations in mapping of glacier parameters from space: results of the 2008 Global Land Ice Measurements from Space (GLIMS) workshop, Boulder, Colorado, USA, Ann. Glaciol., 50, 53–69, https://doi.org/10.3189/172756410790595804, 2009.

Raymond, C. F.: How do glaciers surge? A review, J. Geophys. Res.-Sol. Ea., 92, 9121–9134, https://doi.org/10.1029/JB092iB09p09121, 1987.

Reynaud, L., Vallon, M., and Letreguilly, A.: Mass-Balance Measurements: Problems and two New Methods of Determining Variations, J. Glaciol., 32, 446–454, https://doi.org/10.3189/S0022143000012168, 1986.

RGI 7.0 Consortium: Randolph Glacier Inventory – A Dataset of Global Glacier Outlines, National Snow and Ice Data Center [data set], https://doi.org/10.5067/f6jmovy5navz, 2023.

Riazanoff, S.: SPOT Satellite Geometry Handbook, Tech. Rep. S-NT-73-12-SI, SPOT IMAGE/GAEL Consultant, Toulouse, http://www.engesat.com.br/wp-content/uploads/S-NT-73-12-SI-Geometry-Handbook.pdf (last access: 14 January 2025), 2002.

Round, V., Leinss, S., Huss, M., Haemmig, C., and Hajnsek, I.: Surge dynamics and lake outbursts of Kyagar Glacier, Karakoram, The Cryosphere, 11, 723–739, https://doi.org/10.5194/tc-11-723-2017, 2017.

Savoskul, O.: End of the "Abramov glacier" station, Materialy gliatsiologicheskikh issledovaniy, 88, 233–235, 2000.

Scherler, D., Leprince, S., and Strecker, M.: Glacier-surface velocities in alpine terrain from optical satellite imagery – Accuracy improvement and quality assessment, Remote Sens. Environ., 112, 3806–3819, https://doi.org/10.1016/j.rse.2008.05.018, 2008.

Schöne, T., Zech, C., Unger-Shayesteh, K., Rudenko, V., Thoss, H., Wetzel, H.-U., Gafurov, A., Illigner, J., and Zubovich, A.: A new permanent multi-parameter monitoring network in Central Asian high mountains – from measurements to data bases, Geosci. Instrum. Method. Data Syst., 2, 97–111, https://doi.org/10.5194/gi-2-97-2013, 2013.

Sevestre, H. and Benn, D. I.: Climatic and geometric controls on the global distribution of surge-type glaciers: implications for a unifying model of surging, J. Glaciol., 61, 646–662, https://doi.org/10.3189/2015JoG14J136, 2015.

Shean, D. E., Bhushan, S., Montesano, P., Rounce, D. R., Arendt, A., and Osmanoglu, B.: A Systematic, Regional Assessment of High Mountain Asia Glacier Mass Balance, Frontiers in Earth Science, 7, 363, https://doi.org/10.3389/feart.2019.00363, 2020.

Shugar, D. H., Jacquemart, M., Shean, D., Bhushan, S., Upadhyay, K., Sattar, A., Schwanghart, W., McBride, S., De Vries, M. V. W., Mergili, M., Emmer, A., Deschamps-Berger, C., McDonnell, M., Bhambri, R., Allen, S., Berthier, E., Carrivick, J. L., Clague, J. J., Dokukin, M., Dunning, S. A., Frey, H., Gascoin, S., Haritashya, U. K., Huggel, C., Kääb, A., Kargel, J. S., Kavanaugh, J. L., Lacroix, P., Petley, D., Rupper, S., Azam, M. F., Cook, S. J., Dimri, A. P., Eriksson, M., Farinotti, D., Fiddes, J., Gnyawali, K. R., Harrison, S., Jha, M., Koppes, M., Kumar, A., Leinss, S., Majeed, U., Mal, S., Muhuri, A., Noetzli, J., Paul, F., Rashid, I., Sain, K., Steiner, J., Ugalde, F., Watson, C. S., and Westoby, M. J.: A massive rock and ice avalanche caused the 2021 disaster at Chamoli, Indian Himalaya, Science, 373, 300–306, https://doi.org/10.1126/science.abh4455, 2021.

Smith, S. M. and Brady, J. M.: SUSAN – A New Approach to Low Level Image Processing, Int. J. Comput. Vision, 23, 45–78, https://doi.org/10.1023/A:1007963824710, 1997.

Suslov, V., Akbarov, A., and Emelyianov, Y.: Abramov glacier, Hydrometeoizdat, 207 pp., Leningrad, 1980 (in Russian).

Terleth, Y., Van Pelt, W. J. J., Pohjola, V. A., and Pettersson, R.: Complementary Approaches Towards a Universal Model of Glacier Surges, Frontiers in Earth Science, 9, 732962, https://doi.org/10.3389/feart.2021.732962, 2021.

Thøgersen, K., Gilbert, A., Schuler, T. V., and Malthe-Sørenssen, A.: Rate-and-state friction explains glacier surge propagation, Nat. Commun., 10, 2823, https://doi.org/10.1038/s41467-019-10506-4, 2019.

Toutin, T.: Review article: Geometric processing of remote sensing images: models, algorithms and methods, Int. J. Remote Sens., 25, 1893–1924, https://doi.org/10.1080/0143116031000101611, 2004.

Tyc, G., Tulip, J., Schulten, D., Krischke, M., and Oxfort, M.: The RapidEye mission design, Acta Astronaut., 56, 213–219, https://doi.org/10.1016/j.actaastro.2004.09.029, 2005.

Unger-Shayesteh, K., Vorogushyn, S., Farinotti, D., Gafurov, A., Duethmann, D., Mandychev, A., and Merz, B.: What do we know about past changes in the water cycle of Central Asian headwaters? A review, Global Planet. Change, 110, 4–25, https://doi.org/10.1016/j.gloplacha.2013.02.004, 2013.

U.S. Geological Survey: EarthExplorer, https://earthexplorer.usgs.gov/, last access: 14 January 2025.

van der Veen, C. J.: Fundamentals of glacier dynamics, CRC Press, Boca Raton, FL, second edn., ISBN 978-1-4398-3566-1, 2013.

Van Tricht, L., Paice, C. M., Rybak, O., Satylkanov, R., Popovnin, V., Solomina, O., and Huybrechts, P.: Reconstruction of the Historical (1750–2020) Mass Balance of Bordu, Kara-Batkak and Sary-Tor Glaciers in the Inner Tien Shan, Kyrgyzstan, Frontiers in Earth Science, 9, 734802, https://doi.org/10.3389/feart.2021.734802, 2021.

Van Wychen, W., Davis, J., Burgess, D. O., Copland, L., Gray, L., Sharp, M., and Mortimer, C.: Characterizing interannual variability of glacier dynamics and dynamic discharge (1999–2015) for the ice masses of Ellesmere and Axel Heiberg Islands, Nunavut, Canada, J. Geophys. Res.-Earth, 121, 39–63, https://doi.org/10.1002/2015JF003708, 2016.

Van Wyk de Vries, M. and Wickert, A. D.: Glacier Image Velocimetry: an open-source toolbox for easy and rapid calculation of high-resolution glacier velocity fields, The Cryosphere, 15, 2115–2132, https://doi.org/10.5194/tc-15-2115-2021, 2021.

World Glacier Monitoring Service (WGMS): Fluctuations of Glaciers Database, WGMS [data set], https://doi.org/10.5904/WGMS-FOG-2024-01, 2024.

Xenarios, S., Gafurov, A., Schmidt-Vogt, D., Sehring, J., Manandhar, S., Hergarten, C., Shigaeva, J., and Foggin, M.: Climate change and adaptation of mountain societies in Central Asia: uncertainties, knowledge gaps, and data constraints, Reg. Environ. Change, 19, 1339–1352, https://doi.org/10.1007/s10113-018-1384-9, 2019.

Zemp, M., Huss, M., Thibert, E., Eckert, N., McNabb, R., Huber, J., Barandun, M., Machguth, H., Nussbaumer, S. U., Gärtner-Roer, I., Thomson, L., Paul, F., Maussion, F., Kutuzov, S., and Cogley, J. G.: Global glacier mass changes and their contributions to sea-level rise from 1961 to 2016, Nature, 568, 382–386, https://doi.org/10.1038/s41586-019-1071-0, 2019.

Zheng, W., Bhushan, S., Van Wyk De Vries, M., Kochtitzky, W., Shean, D., Copland, L., Dow, C., Jones-Ivey, R., and Pérez, F.: GLAcier Feature Tracking testkit (GLAFT): a statistically and physically based framework for evaluating glacier velocity products derived from optical satellite image feature tracking, The Cryosphere, 17, 4063–4078, https://doi.org/10.5194/tc-17-4063-2023, 2023.

Zhou, Y., Li, Z., Li, J., Zhao, R., and Ding, X.: Geodetic glacier mass balance (1975–1999) in the central Pamir using the SRTM DEM and KH-9 imagery, J. Glaciol., 65, 309–320, https://doi.org/10.1017/jog.2019.8, 2019.